SGG SGS sc | nat
Swiss Journal of Geosciences

ORIGINAL PAPER Open Access

Early Pleistocene complex cut-and-fill sequences in the Alps

Catharina Dieleman[1*], Marcus Christl[2], Christof Vockenhuber[2], Philip Gautschi[2] and Naki Akçar[1]

Abstract

Cut-and-fill sequences are the result of climatically or tectonically induced alternating aggradation and incision phases of a fluvial system. A recently established cosmogenic nuclide chronology of the Cover Gravels (*Deckenschotter* in German) in the northern Alpine Foreland, which are the oldest Quaternary glaciofluvial gravels and comprise evidence of early Pleistocene glaciations, suggests a cut-and-fill build-up. This suggested cut-and-fill architecture challenges the morphostratigraphy. The Deckenschotter deposits represent a suitable archive for reconstructing drainage patterns, base level changes, and the landscape evolution of the northern Alpine Foreland during the early Pleistocene. In this study, we focused on the highest morphostratigraphic Deckenschotter sites: three at Irchel and one in the area around Lake Constance. Sediment analyses were performed to determine their provenance and depositional environments. The geochronology was established using isochron-burial dating. The results indicate that the sediments were transported from the Central and eastern Central Alps, as well as from the Molasse, to the foreland and deposited in a proximal glaciofluvial environment. Based on these findings, we propose that the Deckenschotter are cut-and-fill sequences that accumulated in three stages during the early Pleistocene at ca. 2.5 Ma, ca. 1.5 Ma, and ca. 1 Ma. The presence of a cut-and-fill system implies that the regional base level was relatively constant during the early Pleistocene. In addition, the ca. 2.5 Ma glaciofluvial gravels document the first evidence of glaciers in the northern Alpine Foreland. This timing is synchronous with the onset of Quaternary glaciation in the northern hemisphere at ca. 2.7 Ma.

Keywords: Deckenschotter, Glaciofluvial deposits, Isochron-burial dating, Swiss northern Alpine Foreland, Cosmogenic nuclides, ^{10}Be and ^{26}Al

1 Introduction

The interactions between stream power and its base level produce either aggradation or incision along the course of a river (e.g., Blum & Törnqvist, 2000; Burbank & Anderson, 2011). For example, aggradation will occur when water discharge is lower and the bedload is higher than during an incision phase (Bull, 1990; Burbank & Anderson, 2011; Howard et al., 1997). Whether rivers aggrade or incise is dependent on changes in climate and/or tectonics (Burbank & Anderson, 2011). Thus, fluvial sequences represent an archive of the evolution of a drainage system, terrace formation, and climate, as well as environmental changes, uplift rates, base-level changes, and changes in hydrological conditions (Bender et al., 2016; Bridgland & Westaway, 2014; Erlanger et al., 2012; Grotzinger & Jordan, 2017; Macklin et al., 2012; Schaller et al., 2016; Schildgen et al., 2002).

Alternating aggradation and incision phases of a river can result in cut-and-fill sequences (Bull, 1990; Burbank & Anderson, 2011; Howard et al., 1997). A simple cut-and-fill sequence can form as follows. During the first phase, the river incises the bedrock or existing valley fill as a result of increased stream power and/or a reduction in bedload. As a result, degradational or strath terraces form. During the second phase, the river accumulates

Editorialhandling: Wilfried Winkler

*Correspondence: catharina.dieleman@geo.unibe.ch
[1] Institute of Geological Sciences, University of Bern, Bern, Switzerland
Full list of author information is available at the end of the article

sediment in the space created by the incision due to a higher bedload and/or reduced stream power. During the third phase, the sediments deposited during the second phase are incised and new accumulation occurs (Burbank & Anderson, 2011; Howard et al., 1997). Such cycles of aggradation and incision can also lead to the burial of older deposits by younger ones, which makes the history of cut-and-fill sequences complex (Lewin & Gibbard, 2010; Richards, 2002). In the study of cut-and-fill sequences, it is important to unravel the processes that produced the cut-and-fill cycles. Terrace formation in cut-and-fill systems has been attributed to either climate change induced by Milankovitch cycles (Bekkaddour et al., 2014; Litty et al., 2018; Huang et al., 2019; Whitfield et al., 2013) or glacial–interglacial cycles (e.g., Bridgland, 2000 and references therein; Schildgen et al., 2002). The formation of cut-and-fill sequences can also be explained by the interplay between tectonics and wet or dry climates (Tofelde et al., 2017). To reconstruct the geochronology is of utmost importance for determining the sequence of events in a cut-and-fill system and to recognize the forces driving the system. Dating techniques that utilize cosmogenic nuclides (e.g., Huang et al., 2019), optically stimulated luminescence (e.g., Egberts et al., 2020), radiocarbon (e.g., Foster et al., 2009), U-Th isotopes (Kock et al., 2009), and biostratigraphy (e.g., White et al., 2017) are widely used to detect terrace chronologies. However, establishing the sequence of events in a cut-and-fill system can be hampered by erosion and weathering of the terrace fills, which leaves behind laterally and vertically discontinuous and fragmented archives (Lewin & Macklin, 2003).

The Quaternary sedimentary records in the Swiss northern Alpine Foreland are laterally and vertically discontinuous (Fig. 1). These archives can be morphostratigraphically attributed to the oldest Quaternary deposits and are classified as "Cover Gravels" (*Deckenschotter* in German). They lie unconformably on top of Cenozoic Molasse or Mesozoic bedrock. Swiss Deckenschotter consist of glaciofluvial sediments intercalated with glacial and/or overbank deposits

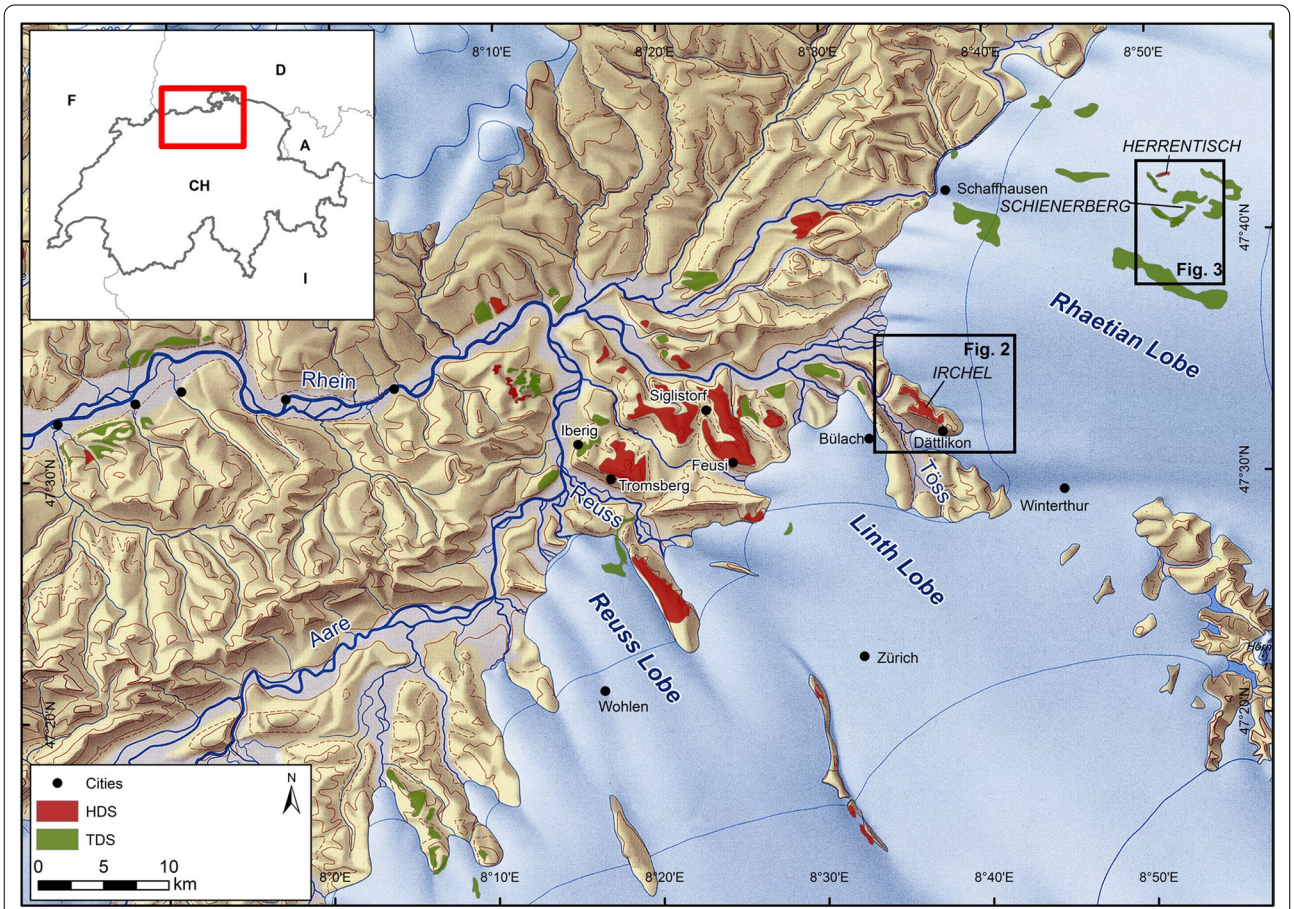

Fig. 1 The extent of the Reuss, Linth, and Rhaetian Lobes in the Swiss northern Alpine Foreland during the Last Glacial Maximum (LGM) (Bini et al., 2009) ©Federal Office of Topography, swisstopo, CH-3084 Wabern. Please note that the Rhaetian Lobe is the merge of the Rhine and Thur paleoglaciers. HDS: Upper Deckenschotter Deposits; TDS: Lower Deckenschotter Deposits. The black rectangles mark the extent of Figs. 2 and 3

(Du Pasquier, 1891; Graf, 1993). Based on their topographic location, Deckenschotter are subdivided into the lithostratigraphic groups Upper Cover Gravels (HDS; *Höhere Deckenschotter* in German) and Lower Cover Gravels (TDS; *Tiefere Deckenschotter* in German) separated by a significant incision phase (Graf & Müller 1999). The different Deckenschotter units are different informal groups and their subdivisions represent informal formations. The HDS and the TDS together with the Higher Terraces (HT; *Hochterrasse* in German), and the Lower Terraces (NT; *Niederterrasse* in German) represent the four distinct morphostratigraphic units, which were introduced based on the observed outwash plains in Bavaria by Penck and Brückner (1909). For a long time these units were correlated with the Günz, Mindel, Riss, and Würm glaciations, whereas the HDS were correlated with the Günz glaciation, the TDS with the Mindel, the HT with the Riss, and the NT with the Würm. Since the identification of the Deckenschotter at the end of the nineteenth century (Du Pasquier, 1891), other than the normal polarity indicated by paleomagnetism (Graf, 1993), the only evidence obtained related to their chronology were mammal fossils found in overbank deposits in the HDS at Irchel (Canton of Zurich) in the 1990s that were attributed to Mammal Neogene 17 (MN17, 1.8–2.5 Ma) (Bolliger et al., 1996). Therefore, the timing of the HDS and TDS remained relatively unconstrained until the last decade, when depth profile and isochron-burial burial dating techniques, as well as burial dating applying the P-PINI method were used to determine the chronostratigraphy of the Swiss Deckenschotter (Akçar et al., 2014, 2017; Claude et al., 2017, 2019; Knudsen et al., 2020). According to these studies, the HDS were deposited between 2.8 Ma and 0.8 Ma and the TDS between 0.7 Ma and 0.5 Ma (Akçar et al., 2014, 2017; Claude et al., 2017, 2019; Knudsen et al., 2020). In addition, three HDS subunits at Irchel indicated that ca. 1 Ma deposits are located at the same topographic elevation as ca. 2 Ma deposits (Claude et al., 2019).

Intercalated till layers within the Deckenschotter deposits (e.g., at Feusi) and sedimentological provenance analyses of various HDS and TDS sites in the Swiss northern Alpine Foreland Basin indicate that these sites were affected by ice lobes that drained the Alpine Ice Sheet during glacial periods (Graf, 1993, 2009). The topographically highest (and morphostratigraphically oldest) HDS deposits are located at Irchel and at Herrentisch, Canton of Schaffhausen (Fig. 1). The Irchel Gravel Complex is built up by five lithostratigraphic formations that overlie the Molasse. Morphostratigraphically, from oldest to youngest, the formations are: the Langacher Gravel, Irchel Gravel, Steig Gravel, Hasli formation, and Forenirchel Gravel (Fig. 2) (Graf, 1993). These gravels were transported by the Linth Lobe (Graf, 1993). The MN17 mammal fossils were found in the Hasli formation, which is consisting of overbank deposits (Bolliger et al., 1996). Therefore, the morphostratigraphically older Langacher, Irchel, and Steig gravels are considered to have been deposited prior to MN17. However, the recently developed cosmogenic nuclide chronology contradicts the existing morphostratigraphy and suggests a more complex cut-and-fill history for the HDS at Irchel (Claude et al., 2019). The ca. 1 Ma old deposits show an influence from the Rhaetian paleoglacier, whereas the older gravel units do not (Claude et al., 2019). This change in petrographic composition was interpreted as a result of the rerouting of the Rhine River during the Mid-Pleistocene Revolution, which is characterized by climatic changes and major changes in drainage patterns (e.g. Clark et al., 2006). The second morphostratigraphically highest Deckenschotter unit after the Irchel area is located at Herrentisch (Fig. 1), which is assumed to be first transported onto the northern Alpine Foreland by the Rhaetian Lobe and then by meltwater discharge (Graf, 2009). Since the deposition of the Deckenschotter in the Lake Constance region the erosional base has been lowered by ca. 280 m (Heuberger et al., 2014).

The goal of this study was to determine whether the Deckenschotter deposits at Herrentisch and Irchel formed as multiple cut-and-fill sequences within the Höhere Deckenschotter, as well as to reconstruct changes in base level and landscape evolution during the early Pleistocene in the northern Alpine Foreland. Therefore, we focused on the following sites at Irchel: Schartenflue (Langacher Gravel), Hochwacht (Irchel Gravel), and Hasli (Steig Gravel), as well as the Chroobach site at Herrentisch (Figs. 2, 3). The deposits at each site were analyzed in detail in the field to reconstruct the provenance of the sediments, the depositional environment, and the paleoflow direction. The geochronology was established using the isochron-burial dating technique with cosmogenic ^{10}Be and ^{26}Al. The sedimentology of the deposits indicated the presence of six units at Irchel. At Chroobach, possible transport by the Rhaetian Lobe (Bini et al., 2009), which includes the Rhine and Thur paleoglaciers, was observed. In addition, the results suggest that Deckenschotter deposits formed by multiple cut-and-fill events that occurred in three stages during the early Pleistocene.

2 Study sites

The Irchel area is a ca. 4.5 km long and 1.5 km wide mesa-type hill in the Swiss northern Alpine Foreland beyond the extent of the Last Glacial Maximum (LGM) (Fig. 1). It is located approximately 20 km NNE of Zurich between the Rhine and Töss rivers. The highest elevation is 694 m a.s.l.. The Miocene Upper Freshwater Molasse (OSM; *Obere Süsswasser Molasse* in German) unconformably underlies the Deckenschotter at Irchel

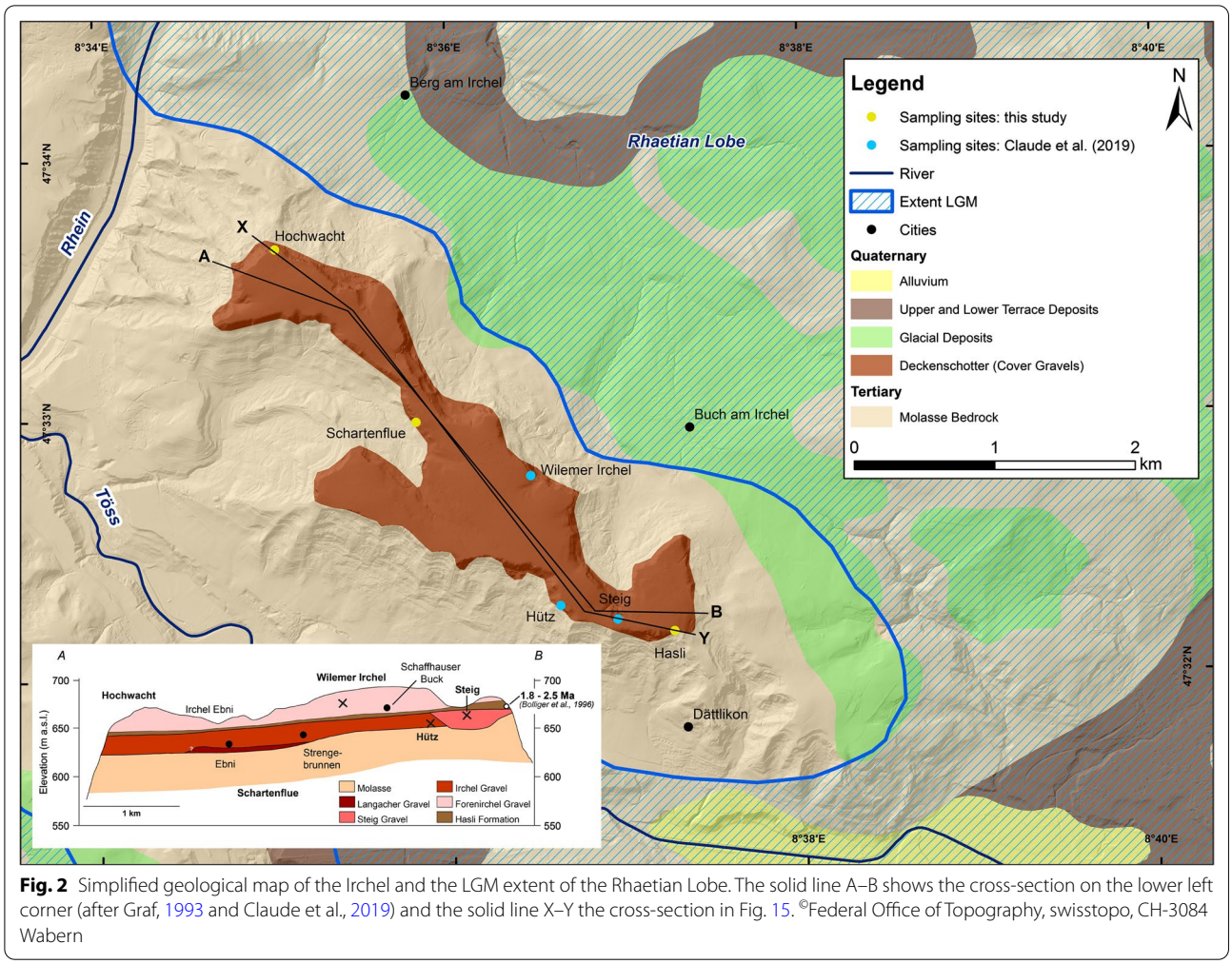

Fig. 2 Simplified geological map of the Irchel and the LGM extent of the Rhaetian Lobe. The solid line A–B shows the cross-section on the lower left corner (after Graf, 1993 and Claude et al., 2019) and the solid line X–Y the cross-section in Fig. 15. ©Federal Office of Topography, swisstopo, CH-3084 Wabern

(Fig. 2). The unconformity between the Deckenschotter and the OSM can be observed at different locations across the Irchel. In the southeastern part, the Deckenschotter has a maximum thickness of 25 m, while it is 40 m thick in the northwestern part. Furthermore, the base of the Deckenschotter decreases from 660 m a.s.l. in the southeast to approximately 625 m a.s.l. in the northwest (Du Pasquier, 1891; Frei, 1912a; Graf, 1993).

The HDS at Irchel was placed into a chronostratigraphic framework using topographical location, paleomagnetism, and biostratigraphy (Fig. 2) (Bolliger et al., 1996; Graf, 1993). The paleomagnetism of the Hasli formation exhibits a trend to an inverse polarity and is therefore older than the Brunhes chron (0.78–0 Ma; Spell & McDougall, 1992). In general the HDS show a normal polarity and therefore, the accumulation should belong to a normal polarity event such as the Jaramillo event (1.01–0.9 Ma) or the Olduvai (2.0–1.78 Ma) during the Matuyama chron (2.6–0.78 Ma; McDougall et al., 1992) (Graf, 1993). In addition, a re-analysis of the mammal fossils (*Arvicolinae*) found in the Hasli formation indicates that they belong to the upper part of the MN17, suggesting an age of ca. 2.0–1.8 Ma (Cuenca-Bescos, 2015). Three sites at Irchel have been dated with cosmogenic nuclides (Claude et al., 2019). The Steig gravel was dated to 0.9 ± 0.2 Ma, while the Irchel Gravel at the Hütz site was dated to 0.9 ± 0.2 Ma using isochron-burial dating. The Forenirchel Gravel at Wilemer Irchel yielded a cosmogenic ^{10}Be depth-profile age of $2.8^{+1.8}_{-1.0}$ Ma (4σ; Claude et al., 2019). According to the morphostratigraphy proposed by Graf (1993), the Forenirchel Gravel is topographically the highest unit at Irchel; thus, it should be younger than the Irchel and Steig gravels. However, the cosmogenic nuclide geochronology indicates a more complex stratigraphy than the proposed morphostratigraphy (Claude et al., 2019).

At Irchel, we investigated the Langacher Gravel at Schartenflue, the Irchel Gravel at Hochwacht, and the Steig Gravel at Hasli (Fig. 2). Schartenflue is located at an elevation of 636 m a.s.l. in the northern part of

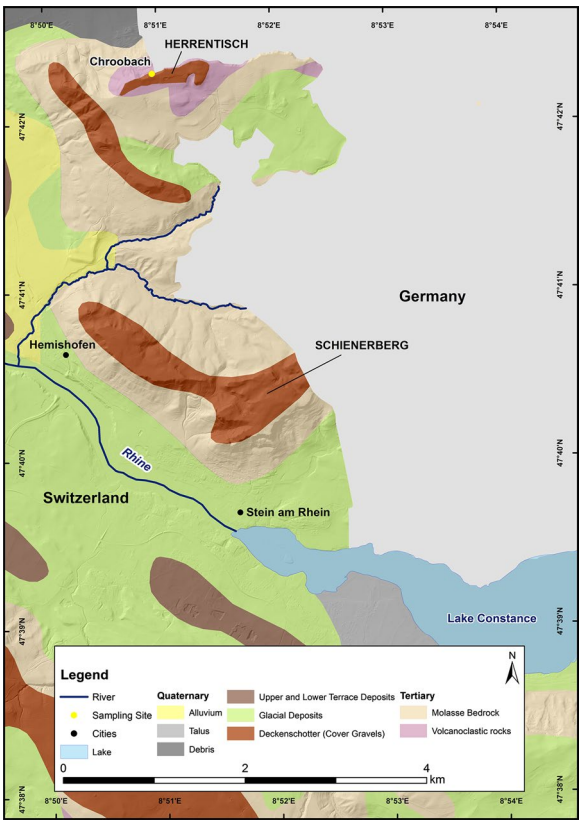

Fig. 3 Simplified geological map of the Lake Constance region. ©Federal Office of Topography, swisstopo, CH-3084 Wabern

the Irchel. At this outcrop, the Langacher Gravel is underlain by the Molasse bedrock and overlain by the Irchel Gravel. The stratigraphic boundary between the Langacher and Irchel gravels consists of a 50 cm thick paleosol that contains heavily weathered non-carbonate clasts (Graf, 1993). The Irchel Gravel that underlies the Hasli Formation was investigated at the Hochwacht site in the northwestern part of Irchel. The Molasse bedrock outcrops approximately 50 m northwest of the outcrop at 637 m a.s.l. The Hasli site is at an elevation of 655 m a.s.l. We studied the Steig Gravel at this site, which is located approximately 10 m below the Hasli Formation (Fig. 2).

The Herrentisch (684 m a.s.l.) is a ca. 2.5 km long by 0.5 km wide mesa-type hill in the Schienerberg area, which is located on the western side of Lake Constance (Fig. 3). The uppermost 10 m of this hill is composed of HDS, which unconformably overlies the Molasse bedrock. In addition, the HDS was covered by the Rhaetian Lobe during the LGM (Fig. 1). In this study, we examined the HDS at the Chroobach site. The sampling site is located at an elevation of 672 m a.s.l. and the base of the HDS sequence is located at approximately 670 m a.s.l. (Frei, 1912a, b; Graf, 2009; Heuberger et al., 2014).

3 Methodology

3.1 Sediment analyses

The analysis of clasts in a deposit provides information about their origin, transport mechanism, and depositional environment (Schlüchter, 1989; Weltje & von Eynatten, 2004). As the Deckenschotter deposits contain clasts of different lithologies, clast petrography establishes their provenance (Adelsberger, 2017; Claude et al., 2017, 2019; Frei, 1912a; Graf, 1993; Lindsey et al., 2007; Schlüchter, 1989; Weltje & von Eynatten, 2004). In the field, a bucket was used to collect gravel samples to avoid any visual bias. At each site, fresh material from the outcrop was collected using the bucket and afterwards sieved into the pebble fraction (2–6 cm). This fraction has been transferred back into the bucket and at least 250 clasts were selected blindly from the bucket (after Schlüchter, 1989). The clasts were petrographically classified into the following lithologies: (1) light colored limestones, (2) dark colored limestones, (3) grey limestones (4) siliceous limestones, (5) vein quartz, (6) quartzites, (7) chert/hornstones, (8) radiolarites, (9) sandstones, (10) dolomites, and (11) crystallines (Claude et al., 2017; Graf, 1993, 2009; Schlüchter, 1989). In addition, key lithologies were identified. For example, the Verrucano, a red colored conglomerate and breccia, is a key lithology for the Linth Lobe (Hantke, 1980), while the Julier granite is a key lithology for the Rhine and Thur Lobes. We looked explicitly for these two lithologies to gather information on the ice lobes that transported these sediments.

Clast morphology is particularly suited to define glacial and fluvial transport (Benn, 2004). Over time, different methods have been developed to analyze clast morphologies (Benn, 2004; Cailleux, 1947; Sneed & Folk, 1958). Sneed and Folk (1958) assessed each clast based on roundness, sphericity, and form. Benn and Ballantyne (1994) suggested the C_{40}-index (percentage of clasts with a ratio of c/a-axis ≤ 0.4) to interpret clast forms combined with the RA-index (percentage of angular and very angular clasts) or the RWR-index (percentage of rounded and well-rounded clasts). The RA-C_{40} index is applied mostly in glacial settings because it can differentiate between supraglacially-transported angular clasts and subglacially-transported abraded clasts (Benn & Ballantyne, 1994; Benn, 2004; Brook & Lukas, 2012). The RWR-C_{40} index, which targets the more rounded clasts, is more suitable in some settings for distinguishing between different transport mechanisms (Benn, 2004; Brook & Lukas, 2012; Evans et al., 2010; Lukas et al., 2013). To analyze the morphometry of the gravels at the study sites, we applied the technique proposed by Cailleux, (1947) because the reported shapes of the clasts in the Deckenschotter deposits at Irchel were sub-angular to sub-rounded (Graf, 1993). This method has been applied

in glacial and meltwater environments (Cailleux, 1947; Schlüchter, 1989). To obtain significant results and exclude the effect of lithology on the shape of the clasts during transport, clasts from the same lithology must be analyzed (Benn, 2004; Schlüchter, 1989). In this study, at least 100 vein quartz clasts from the gravel fraction were collected at each site to determine the flattening and roundness indices.

The clast fabric provides information about the depositional environment and the transport mechanism (Boulton, 1978; Benn & Ballantyne, 1994; Benn, 2004; Lukas et al., 2012; Sneed & Folk, 1958). As clast fabric also includes a description of the orientation of single clasts in sediment, this analysis allows the reconstruction of paleoflow direction (Adelsberger, 2017; Boggs, 2009; Chandler & Hubbard, 2008; Lukas et al., 2012;). Therefore, elongated clasts are of particular interest (Boggs, 2009). To determine the paleoflow direction, clasts with an a-axis > 6.3 cm and a b:a ratio of > 1.5 were used (Lukas et al., 2012). A ratio of > 1.5 ensures that elongated clasts are measured, but not oblate clasts. In the field, the azimuth and inclination of the 25 clasts that fulfilled these criteria were measured.

3.2 Isochron-burial dating

Isochron-burial dating is used to determine the timing of deposition of terrestrial sequences, such as river terraces, glaciofluvial sediments, or paleosols, for a time range of 0.1–5 Ma (Akçar et al., 2017; Balco & Rovey, 2008; Balco et al., 2013; Bender et al., 2016; Çiner et al., 2015; Claude et al., 2017, 2019; Darling et al., 2012; Erlanger et al., 2012; Litty et al., 2018; Matmon et al., 2015; Schaller et al., 2016; Tu et al., 2017; van Buuren et al., 2020; Zhao et al., 2016). This method is based on the radioactive decay of cosmogenic ^{10}Be ($t_{1/2} = 1.4$ Ma) and ^{26}Al ($t_{1/2} = 0.7$ Ma) (Akçar et al., 2017; Balco & Rovey, 2008; Bender et al., 2016; Erlanger et al., 2012). The isochron-burial dating method takes advantage of the difference in the ^{26}Al/^{10}Be ratio at the surface at the time of deposition and the ^{26}Al/^{10}Be ratio of the deposit to calculate a depositional age (Akçar et al., 2017; Balco & Rovey, 2008; Bender et al., 2016; Erlanger et al., 2012). This method can be applied to sediments with a more complex exposure history prior to burial and experienced post-burial production (Akçar et al., 2017; Balco & Rovey, 2008; Bender et al., 2016; Granger & Muzikar, 2001). Samples from the same chronozone that share the same post-burial histories and differences in inherited nuclide concentrations (i.e., different pre-burial histories) are crucial for calculating isochron-burial ages (Akçar et al., 2017; Balco et al., 2013; Bender et al., 2016; Çiner et al., 2015; Claude et al., 2019; Erlanger et al., 2012; Schaller et al., 2016).

3.2.1 Sampling and sample preparation

A total of 49 samples from 4 sites were collected (Table 1). At each site, the coordinates of the sampling locations were determined using a GPS and the altitudes were taken from the high resolution digital maps, made publicly available by the Federal Office of Topography (swisstopo), because they are more accurate compared to the ones measured by the GPS. At each site, at least nine clasts and a sediment sample consisting of > 50 quartz pebbles were collected. To ensure a variety of pre-burial histories, we collected clasts of different lithologies, shapes, and sizes. Thirteen clasts (quartzite, vein quartz, and Verrucano) were collected at Hasli, nine clasts (quartzite, vein quartz, and sandstone with quartz veins) were collected at Hochwacht, 11 clasts (quartzite, vein quartz, gneiss, and conglomerate) were collected at Schartenflue, and 12 clasts (quartzite) were collected at Chroobach.

The sample preparation for cosmogenic ^{10}Be and ^{26}Al analyses took place at the Surface Exposure Laboratory of the University of Bern. For each study site, we first prioritized nine clasts and the sediment samples and purified them according to the methods described by Akçar et al., (2017 and references therein). We aimed for approximately 50 g of pure quartz. To achieve high quality ^{26}Al/^{27}Al accelerator mass spectrometry (AMS) measurements a maximum Al concentration of 30 ppm was targeted prior to dissolution (Akçar et al., 2017; Claude et al., 2019). Total Al concentrations were measured before dissolving the samples. Samples that exceeded the targeted Al concentration were either subjected to additional leaching steps or excluded. The samples fulfilling the requirements were dissolved in batches of nine samples and a full process blank. Twenty-seven samples between 45 and 50 g were dissolved. Each sample was spiked with ca. 200 µl of Be carrier and the full process blank with 400 µl (Table 2). The cosmogenic ^{10}Be und ^{26}Al were extracted based on the protocols described by Akçar et al., (2017), after which the ^{10}Be/^{9}Be ratios and ^{26}Al/^{27}Al ratios were measured at the AMS facilities at ETH Zurich. Cosmogenic ^{10}Be/^{9}Be ratios of five samples from the Hochwacht site were measured using the TANDY accelerator (Christl et al., 2013; Müller et al., 2010). The ^{10}Be/^{9}Be of 20 samples and the ^{26}Al/^{27}Al ratios of all samples were measured using the MILEA accelerator (Maxeiner et al., 2019). All measured ^{10}Be/^{9}Be ratios were normalized to the ETH Zurich in-house standards S2007N and S2010N (Christl et al., 2013) and corrected with a weighted average full process blank ratio of $(2.76 \pm 0.18) \times 10^{-15}$. The total Al concentrations were determined using inductively coupled plasma optical emission spectrometry (ICP-OES) at the Institute of Geological Sciences of the University of Bern. The ^{26}Al/^{10}Be

Table 1 Sample information for the Deckenschotter sites investigated in this study

Site	Sample name	Lithology	Altitude (m a.s.l.)	Latitude (°N) (DD.DD)	Longitude (°E) (DD.DD)	Amount of quartz after leaching (g)	Amount of Al after leaching (ppm)
Irchel Hasli	HASL-1	Quartzite	655	47.5346	8.6200	81	65
	HASL-2	Quartzite				64	39
	HASL-3	Quartzite				85	109
	HASL-5	Quartzite				59	151
	HASL-7	Vein quartz				71	20
	HASL-9	Quartzite				77	240
	HASL-10	Quartzite				74	40
	HASL-12	Verrucano				51	157
	HASL-13	Vein quartz				87	25
	HASL-14[a]	qtz pebbles				66	59
Irchel Hochwacht	HWT-1	Quartzite	637	47.5596	8.5825	76	26
	HWT-2	Vein quartz				81	28
	HWT-3	Quartzite				100	53
	HWT-4	Sandstone				52	57
	HWT-5	Quartzite				70	7
	HWT-6	Quartzite				79	291
	HWT-7	Sandstone				60	138
	HWT-8	Vein quartz				81	27
	HWT-9	Quartzite				51	37
	HWT-10[a]	qtz pebbles				77	25
Irchel Schartenflue	SART-1	Quartzite	636	47.5484	8.5956	80	29
	SART-3	Vein quartz				87	28
	SART-4	Vein quartz				66	6
	SART-5	Quartzite				59	23
	SART-6	Conglomerate				75	148
	SART-7	Quartzite				77	165
	SART-8	Quartzite				66	32
	SART-9	Gneiss				71	32
	SART-10	Vein quartz				47	13
	SART-12[a]	qtz pebbles				51	17
Chroobach	CHRO-1	Quartzite	672	47.70378	8.84923	48	159
	CHRO-2	Quartzite				67	135
	CHRO-3	Quartzite				134	178
	CHRO-4	Quartzite				1	n.a
	CHRO-5	Quartzite				119	146
	CHRO-6	Quartzite				40	250
	CHRO-7	Quartzite				82	157
	CHRO-8	Quartzite				35	149
	CHRO-9	Quartzite				55	138
	CHRO-10	Quartzite				27	N.D
	CHRO-11	Quartzite				53	161
	CHRO-12	Quartzite				n.a	n.a
	CHRO-13[a]	qtz pebbles				46	47

[a] Sediment sample

Table 2 Cosmogenic ^{10}Be and ^{26}Al results of the samples from the sites investigated in this study

Site	Sample name	Quartz dissolved (g)	^{9}Be spike (mg)	^{10}Be/^{9}Be ($\times 10^{-14}$)	Relative uncertainty (%)	Blank correction (%)	^{10}Be concentration ($\times 10^{3}$ atoms/g)	Total Al (ppm)	Total Al (mg)	^{26}Al/^{27}Al ($\times 10^{-14}$)	Relative uncertainty (%)	^{26}Al concentration ($\times 10^{3}$ atoms/g)	^{26}Al/^{10}Be
Irchel Hasli	HASL-1	49.9245	0.1994	4.74	7.1	5.2	11.92 ± 0.90	59	2.94	3.12	4.5	41.01 ± 1.84	3.42 ± 0.30
	HASL-2	50.0278	0.1982	4.18	5.9	5.9	10.34 ± 0.66	20	1.02	16.32	3.5	74.27 ± 2.60	7.18 ± 0.52
	HASL-3	50.1341	0.1973	29.33	2.9	0.8	76.41 ± 2.24	112	5.60	12.11	3.2	301.85 ± 9.66	3.95 ± 0.17
	HASL-7	49.9194	0.2007	5.80	8.8	4.3	14.83 ± 1.38	21	1.04	14.74	3.2	68.50 ± 2.18	4.60 ± 0.45
	HASL-10	50.0306	0.1993	4.88	7.5	5.1	12.26 ± 0.97	46	2.30	5.48	4.2	56.35 ± 2.39	4.57 ± 0.41
	HASL-13	49.9490	0.2001	3.88	8.3	6.4	9.65 ± 0.86	21	1.06	11.23	3.4	53.05 ± 1.80	5.46 ± 0.52
	HASL-14[a]	49.7104	0.1999	4.66	7.8	5.3	11.77 ± 0.98	60	2.99	3.13	4.2	42.02 ± 1.78	3.55 ± 0.33
Irchel Hochwacht	HWT-1[b]	49.9905	0.1987	4.84	8.3	5.1	12.12 ± 1.07	27	1.33	11.42	3.0	67.98 ± 2.07	5.57 ± 0.52
	HWT-2[b]	49.8740	0.1985	8.79	5.6	2.8	22.63 ± 1.30	26	1.29	16.22	2.8	93.82 ± 2.64	4.13 ± 0.26
	HWT-5[b]	50.0044	0.2003	5.09	8.4	4.9	12.89 ± 1.14	6	0.32	50.68	3.2	72.55 ± 2.34	5.60 ± 0.53
	HWT-8[b]	49.9645	0.1970	4.66	7.7	5.3	11.55 ± 0.95	29	1.46	11.30	3.2	73.46 ± 2.33	6.32 ± 0.55
	HWT-10[a,b]	49.9821	0.1940	5.22	6.9	4.7	12.83 ± 0.94	23	1.13	15.56	2.7	78.37 ± 2.14	6.07 ± 0.47
Irchel Scharten-flue	SART-1	49.4902	0.2004	3.54	8.9	7.0	8.82 ± 0.85	25	1.26	8.81	3.4	49.97 ± 1.72	5.62 ± 0.57
	SART-3	49.9366	0.2000	5.14	7.0	4.8	13.01 ± 0.96	29	1.43	10.86	2.8	69.59 ± 1.97	5.32 ± 0.42
	SART-4	50.3363	0.2011	3.95	9.7	6.3	9.80 ± 1.03	6	0.32	37.75	4.1	53.59 ± 2.20	5.43 ± 0.61
	SART-5	50.3356	0.2007	3.25	9.4	7.6	7.92 ± 0.81	25	1.27	7.74	3.9	43.44 ± 1.68	5.44 ± 0.59
	SART-8	49.9562	0.1988	14.25	4.8	1.7	37.16 ± 1.82	33	1.63	19.64	2.7	142.78 ± 3.84	3.83 ± 0.21
	SART-9	49.9853	0.1961	7.25	4.7	3.8	18.29 ± 0.89	31	1.53	15.52	3.1	106.01 ± 3.29	5.80 ± 0.34
	SART-10	45.2778	0.1997	4.67	7.8	5.3	12.96 ± 1.07	11	0.49	32.30	3.8	77.25 ± 2.94	5.92 ± 0.54
	SART-12[a]	48.3244	0.1982	7.00	6.9	3.5	18.43 ± 1.33	20	0.96	17.77	3.3	78.68 ± 2.63	4.25 ± 0.34
Chroobach	CHRO-1	48.3019	0.2000	51.76	2.4	0.5	142.45 ± 3.44	169	8.18	9.97	1.9	376.77 ± 7.16	2.64 ± 0.08
	CHRO-2	49.9828	0.1994	5.62	4.7	4.9	14.23 ± 0.70	141	7.06	2.88	4.1	90.81 ± 3.72	6.38 ± 0.41
	CHRO-5	50.0303	0.1996	7.83	4.3	3.5	20.13 ± 0.90	141	7.07	4.57	3.3	144.11 ± 4.76	7.16 ± 0.40
	CHRO-7	49.9929	0.2002	115.48	1.7	0.2	308.28 ± 5.25	162	8.10	29.50	1.1	1066.03 ± 11.73	3.46 ± 0.07
	CHRO-9	50.0457	0.1984	12.44	4.3	2.2	32.23 ± 1.42	139	6.95	6.77	2.9	209.72 ± 6.08	6.51 ± 0.34
	CHRO-11	49.9865	0.2026	18.65	3.4	1.5	49.77 ± 1.72	191	9.53	5.86	2.7	249.66 ± 6.74	5.02 ± 0.22
	CHRO-13[a]	45.1077	0.1996	14.73	3.3	1.9	42.74 ± 1.44	67	3.01	15.77	2.9	234.61 ± 6.80	5.49 ± 0.24

Accelerator mass spectrometry (AMS) measurement errors are at 1 s level, including the statistical (counting) error and the error due to normalization of standards and blanks. The error weighted average ^{10}Be/^{9}Be full-process blank ratio is $(2.76 \pm 0.18) \times 10^{-15}$. ^{26}Al/^{10}Be ratios were calculated with the CRONUS-Earth exposure age calculator and were referenced to 07KNSTD (http://hess.ess.washington.edu/math/(v.2.3; Balco et al., 2008 and update from v. 2.2 to v. 2.3 published by Balco in June 2016)

[a] Sediment sample

[b] Measured at the TANDY facility

ratios were calculated using the CRONUS-Earth exposure age calculator and referenced to 07KNSTD (Balco et al., 2008, and the update from v. 2.2 to v. 2.3 published by Balco in June 2016; http://hess.ess.washington.edu/math/v.2.3).

We calculated the isochron-burial ages with the MatLab® code provided by Erlanger et al., (2012; in personal communication with Darryl Granger). The code first plotted the measured ^{26}Al concentrations versus the ^{10}Be. Then, it regressed a line through the data plot and estimated a preliminary isochron-burial age by using the slope of the regressed line and its shift from the initial surface production ratio. Then, the code used this preliminary age to determine the post-burial component, which was later deducted from the measured concentrations to compute the inherited isotope concentrations. In the next step, the code corrected the inherited concentrations for the decay of ^{10}Be and ^{26}Al to determine the pre-burial erosion rates, and subsequently calculated an inherited ^{26}Al/^{10}Be ratio. By using the inherited isotope ratios, the code estimated a linearization factor to perform the corrections for post-burial production. Finally, the code plotted the ^{10}Be and ^{26}Al concentrations corrected for post-burial production, recalculated the isochron-burial age and iterated these steps until the age converged. For the isochron-burial age calculations, 1σ AMS measurement uncertainties were considered. To calculate the isochron-burial ages, we applied 4.00 ± 0.32 atoms/gSiO_2/a as the production rate of cosmogenic ^{10}Be at the surface due to spallation at sea level-high latitude (SLHL) (Borchers et al., 2016). Altitude/latitude scaling of the surface production rate was calculated according to the time dependent Lal (1991)/Stone (2000) scheme (Lm). Mean lives of 2.005 Ma for ^{10}Be and 1.02 Ma for ^{26}Al were assumed. ^{10}Be and ^{26}Al half-lives of 1.387 Ma (Chmeleff et al., 2010; Korschinek et al., 2010; Nishiizumi, 2004; Nishiizumi et al., 2007) and 0.705 Ma (Norris et al., 1983), respectively, were used. The surface production ratio of 6.75 is commonly used to determine isochron-burial ages in fluvial settings (e.g. van Buuren et al., 2020 among others) because fluvial erosion gathers the clasts from the surface or near the surface, and this equalizes the initial ratio to the surface ratio. Whereas deep erosion in glacial settings makes the initial ratio equal to the ratio at depth (Akçar et al., 2017). Muon induced reactions dominate the subsurface ^{10}Be and ^{26}Al production and ^{26}Al/^{10}Be ratios at depth up to 8.3 were already reported in the literature (e.g. Braucher et al., 2011, 2013; Margreth et al., 2016). Here, we concisely clarify why the ratio at depth (as initial ratio) is necessary for the isochron-burial age calculations in glacial landscapes. Glaciers deeply erode the bedrock (cf. Fig. 7 in Akçar et al., 2017). The clasts, which are plucked from the depth, are then transported as englacial or subglacial sediment loads. Thus, they are fully isolated from the cosmic ray cascade. Until their deposition in the glacial or glaciofluvial environment, they have never get exposed to the cosmic rays and keep their ratio at depth, which is larger than 6.75. As the original plucking depth remains unknown, Akçar et al., (2017) recommended to use the production ratio at depth, which is ranging from 6.75 to 8.4, for the modelling isochron-burial ages in landscapes dominated by deep erosion. Similarly, the majority of the modeled initial ^{26}Al/^{10}Be ratios at the source, which were computed by a source to sink approach (P-PINI: Particle Pathway Inversion of Nuclide Inventories), were larger than 7.2 (cf. Figure 8 in Knudsen et al., 2020). Knudsen et al. (2020) proposed that the analyzed samples stem from a landscape dominated by fast and deep glacial erosion. In line with these indications, we applied an initial ^{26}Al/^{10}Be ratio of 7.6 ± 0.8 for calculating our isochron-burial ages. In addition, to enable comparison, we also calculated isochron-burial ages for the Feusi, Iberig, and Tromsberg sites based on the reported ^{10}Be and ^{26}Al concentrations in the supplementary file of Knudsen et al. (2020).

4 Results

4.1 Sediment analyses

4.1.1 Gravels at the study sites

At Schartenflue, the Langacher Gravel is 2 m thick and 12 m wide (Fig. 4a), comprising a sandy, uncemented, moderately sorted, and clast-supported gravel (Fig. 4b–d). Sand and silt fractions fill the pore spaces. The cobbles have a maximum size of 25 cm. The upper and lower parts of the gravel layer contain large clasts of up to 25 cm, of which a paleoflow direction towards the NNW was obtained. The middle part is mainly composed of clasts smaller than 6.3 cm and exhibits an imbrication towards the SSE. The contact between the Langacher and the Irchel gravels is a ca. 15 cm thick heavily weathered paleosol layer. The Irchel Gravel at this site is well cemented (Fig. 4a).

The Irchel Gravel at Hochwacht is approximately 6 m thick. Approximately 50 m north of the outcrop, the contact between the Deckenschotter and the underlying Upper Freshwater Molasse (OSM) is visible. The Irchel Gravel at this site is a poorly sorted and poorly cemented sandy gravel, and the grain size ranges up to 20 cm (Fig. 5a). The fabric is mainly clast supported. The matrix mainly comprises sand and a small amount of silt. A paleoflow direction towards the NW was obtained at this site. The Irchel Gravel is overlain by a ca. 1 m thick ochre-colored fine-grained sediment layer that is attributed to the Hasli Formation (Graf, 1993).

At the Hasli site, the ca. 2.5 m thick Steig Gravel outcrops approximately 10 m below the Hasli formation,

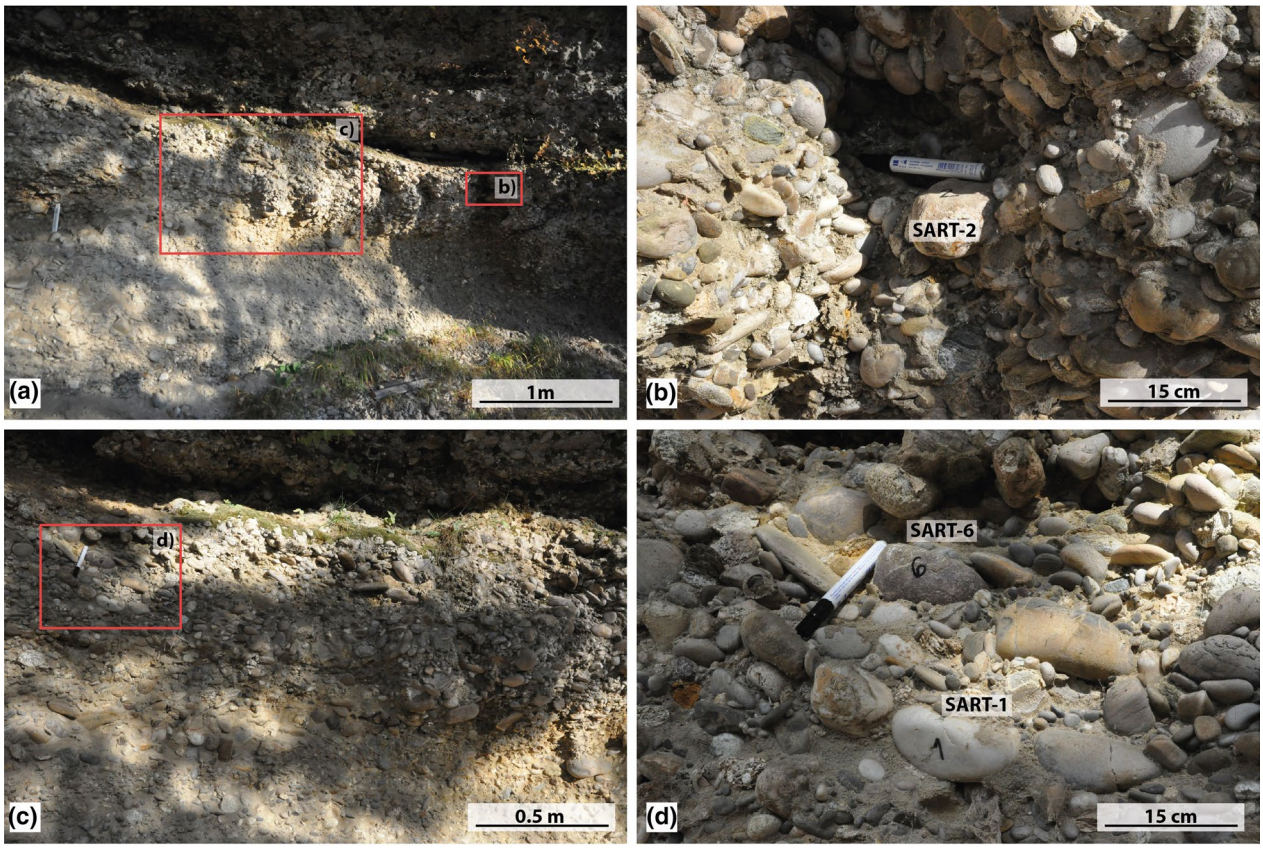

Fig. 4 Field photographs of the Schartenflue site. **a** Overview of the outcrop and positions of the close-up photographs **b** and **c**. **b** Photograph of the sample SART-2. **c** Close-up photograph of the Langacher Gravel and the position of close-up photograph **d**. **d** Photographs of the samples SART-6 and SART-1

where the mammal fossils were found by Bolliger et al. (1996). In a 1.3 m high and 4 m wide cave, unconsolidated and uncemented sandy gravels were observed (Fig. 6a). In the lowermost 20 cm of the gravel layer, poorly sorted clasts of up to 20 cm in diameter were measured (Fig. 6b–d). The remaining gravels are sandy, fine grained, and moderately sorted (Fig. 6a). The matrix filling the spaces consists mainly of fine-grained sand and silt. A N–NNW paleoflow direction was obtained at this site.

At the Chroobach site, the Deckenschotter deposit outcrops along a hiking path and is approximately 4 m in thickness and approximately 15 m in length (Fig. 7a). The gravels are very well cemented (Fig. 7b). The clasts are poorly sorted and have a maximum grain size of approximately 25 cm (Fig. 7b). The matrix is mainly composed of sand and a small amount of silt. A paleoflow direction towards the W/NW was inferred at this site.

4.1.2 Clast petrography

The results of the petrographic analysis performed on clasts from the study sites are shown in Figs. 8 and 9. More than one third of the 279 clasts from Schartenflue are dark colored limestone (37%) (Fig. 8). The second largest relative abundance are quartzite (16%), followed by crystalline clasts (14%). The relative abundances of light colored limestones and siliceous limestone pebbles are the same (9%). Sandstone (6%) and vein quartz clasts (6%) also exhibit the same relative abundances. Chert comprises 2% of the clasts and 1% are radiolarites, while 1% of the clasts are conglomerates, including Verrucano clasts and other conglomerates. At the Hochwacht site, 261 clasts were analyzed (Fig. 8). The limestone aggregates comprise approximately 75%. Of these, 47% are dark colored limestones, 28% are light colored limestones, and 6% are siliceous limestones. Vein quartz and quartzite clasts comprise 7% and 5%, respectively. The same relative abundances are exhibited by sandstones (3%) and crystalline clasts (3%). Conglomerates comprise 2% of the clasts, including Verrucano clasts. One radiolarite

Fig. 5 Field photographs from the Hochwacht site. **a** Overview of the outcrop and the position of photograph **b**. **b** Photograph of the sample HWT-2

clast is found in this set, which is not represented in the pie diagram. At the Hasli site, 274 clasts are analyzed (Fig. 8). The gravels are mostly composed of dark colored limestones (22%) and siliceous limestones (19%). Light colored limestones represent 14% of the clasts. Dolomite (10%), quartzite (11%), and vein quartz (12%) have similar abundances. Sandstone comprise 7% of the clasts. The contribution of crystalline clasts is 3% and chert clasts contribute 1%. Verrucano conglomerate clasts have a relative abundance of 1%. Few radiolarite clasts are found, but their abundance is too small (< 1%), thus they are not shown in the pie diagram. At the Grossrüti site a total of 251 clasts were analyzed, whereof 34% are dark colored limestones (Fig. 8). The siliceous limestones (14%) represent the second largest relative abundance followed by the crystalline (13%). Vein quartz and quartzite show the same relative abundance of 11%. Light colored limestones account for 8% and cherts for 5%. Sandstone clasts comprise 2%. The same relative abundance were exhibited by radiolarite and dolomites (1%). A total of 276 clasts were analyzed from the upper part of the abandoned gravel pit at Strengebrunnen (Fig. 8). Almost half of the clasts are dark colored limestones (42%) and the second largest relative abundance represents siliceous limestones (14%). The contribution of the quartzite is 13% and the one of the crystalline clasts 12%. Vein quartz contributes with 5%. Light colored limestones and sandstones have a relative abundance of 4% each. Cherts and conglomerates contribute with 3% and 2%, respectively. At Chroobach, 259 clasts are analyzed (Fig. 9). Different types of limestone are identified, which aggregate to approximately 80%. Greyish colored limestones represent 40% of the clasts. Dark colored limestones and dolomites have similar relative abundance of 18% and 12%, respectively. Siliceous limestones have a relative abundance of 8% and light colored limestones have an abundance of 3%. The contributions of red colored quartz-rich sandstones and quartzites are 7% and 3%, respectively. Vein quartz and sandstone clasts have the same relative abundances of 1%. Crystalline lithologies represent 3% of the clasts. Chert clasts and weathered components have relative abundances of 2% each. One radiolarite clast is found at this site that is not represented in the pie diagram.

4.1.3 Clast morphometry

At Schartenflue, 114 vein quartz clasts were analyzed for their morphometry (Figs. 10, 11). The roundness indices (Z_i) change from 50 to 600, with some outliers between 650 and 700 (Fig. 10a). The median Md(Z_i) has a value of 253. The distribution is unimodal and has a peak between 200 and 300. The flattening indices (A_i) were between 100 and 400 and had a median Md(A_i) of 168 (Fig. 11a). At Hochwacht, 110 vein quartz clasts were measured. The calculated roundness indices (Z_i) at this site vary from 50 to 600, with a few outliers between 850 and 900. The median Md(Z_i) has a value of 298 (Fig. 10b). The distribution in the histogram is bimodal. The first mode is between 250 and 300, and the second is between 350 and 400. The A_i values range from 100 to 350 and the median Md(A_i) has a value of 174 (Fig. 11b). The 102 vein quartz clasts from Hasli have Z_i values between 100 and 600 and a median Md(Z_i) of 285 (Fig. 10c). The histogram shows a multi-modal distribution. The first mode value is between 200 and 300, the second between 350 and 400, and the third between 450 and 500. The flattening indices (A_i) at Hasli vary between 50 and 350. The median Md(A_i) has a value of 176 (Fig. 11c). The 97 analyzed vein quartz clasts from the Grossrüti site have Z_i values between 50 and 700 and a median Md(Z_i) of 223 (Fig. 10d). The distribution is multimodal with the first peak between 100 and 150, the second one between 200 and 250, and the third one between 350 and 450. The flattening indices (A_i) are between 100 and 300 and have a median Md(A_i) of 174 (Fig. 10d). At Strengebrunnen 108 vein quartz clasts were analyzed. The Z_i values change from 50 to 650 (Fig. 10e). The distribution is unimodal with the peak between 150

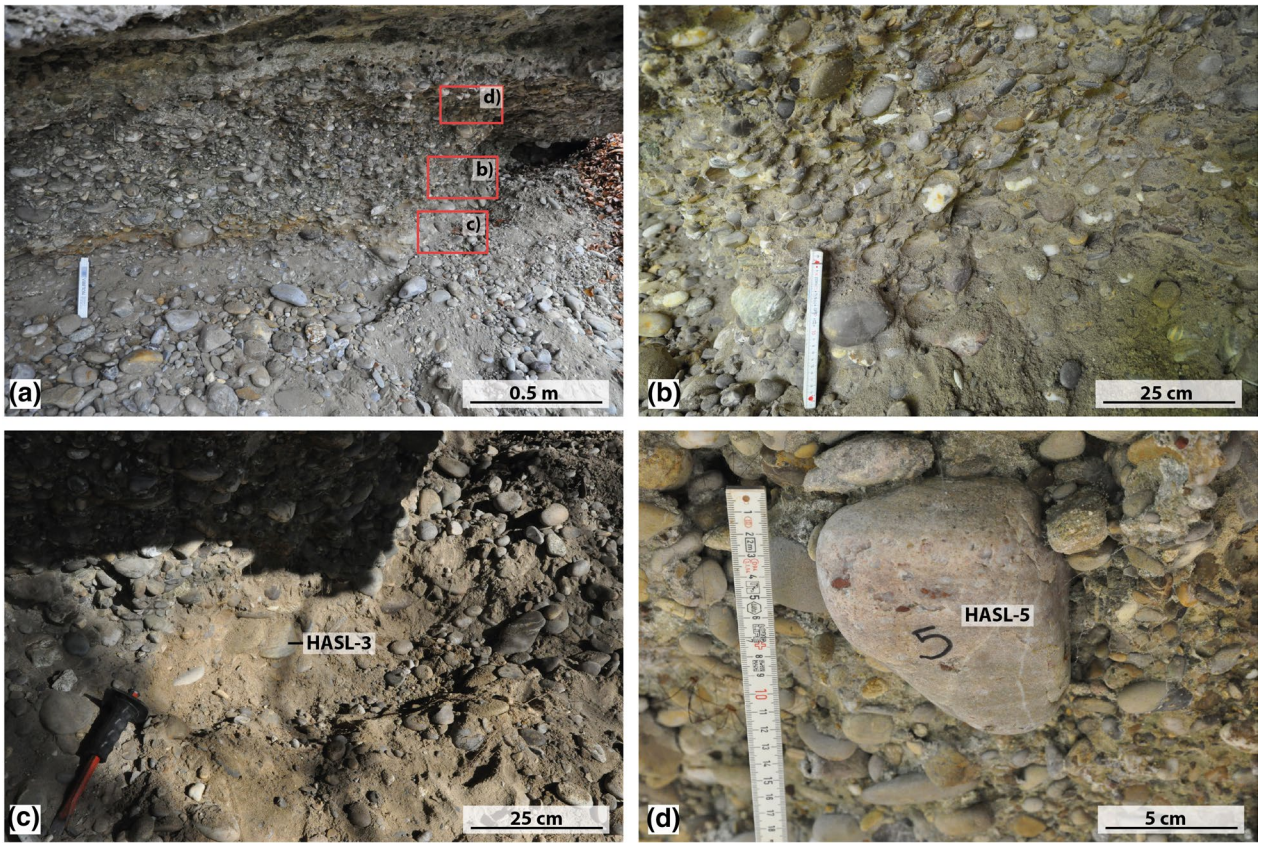

Fig. 6 Field photographs from the Hasli site. **a** Overview of the outcrop and indicating the positions of photographs **b**, **c**, and **d**. **b** Close-up photograph of the Steig Gravel at Hasli showing the poor sorting and the sandy to silty matrix. **c** Photograph of the sample HASL-3. **d** Photograph of the sample HASL-5

and 200. The median Md(Z_i) has a value of 208. The flattening indices (A_i) at Strengebrunnen vary between 100 and 450. The median Md(A_i) has a value of 165 (Fig. 11e). At Chroobach, 112 quartzite clasts were measured. The Zi values range from 50 to 700, with some outliers between 750 and 800. The median Md (Z_i) has a value of 234 (Fig. 10f). The distribution is unimodal, with one mode between 150 and 250. The value of the flattening index (A_i) amounts from 100 to 500, with some outliers between 650 and 700. The median Md(A_i) has a value of 190 (Fig. 11f). The median of the flattening and roundness indices are plotted for the study sites in an A_i-Z_i plot (Fig. 12). These results indicate that the Hasli and Hochwacht sites were located at a transition from glacial to fluvial transport, whereas a larger glacial influence is inferred at the Schartenflue site. The Chroobach, Grossrüti, and Strengebrunnen sites were even more glacially influenced.

4.2 Isochron-burial dating

At total of 27 samples were processed to extract cosmogenic ^{10}Be and ^{26}Al. Eight samples from the Schartenflue site yielded total Al concentrations of 35 ppm and lower (Table 1). The samples were three quartzite clasts (SART-1, SART-5, and SART-8), three vein quartz clasts (SART-3, SART-4, and SART-10), one gneiss clast (SART-9), and one sediment sample (SART-12). At Hochwacht, six out of the ten samples had total Al concentrations below 35 ppm. The sediment sample (HWT-10), two quartzite clasts (HWT-1 and HWT-5), and two vein quartz clasts (HWT-2 and HWT-8) with the lowest Al concentrations were dissolved for the extraction (Table 1). For the Hasli site, three vein quartz clasts (HASL-2, HASL-7, and HASL-13) and one quartzite clast (HASL-10) had the required low total Al concentrations (< 50 ppm) for further processing (Table 1). In addition, the sediment sample (HASL-14) and two quartzite clasts (HASL-1 and HASL-3) were processed, despite having > 50 ppm total Al concentrations. At Chroobach, the sediment sample (CHRO-13) had the necessary low

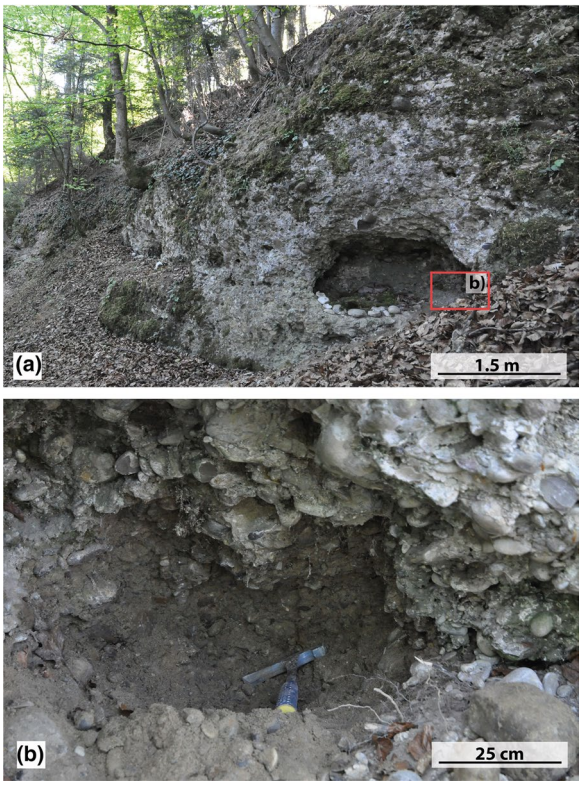

Fig. 7 Field photographs from the Chroobach site. **a** Overview of the well-cemented gravel outcrop along the hiking path and position of photograph **b**. **b** Close-up photograph indicating the uncemented poorly-sorted gravels

total Al-concentrations (Table 1). As it was not possible to reduce the total Al concentrations in the other samples by applying multiple leaching steps, six quartzite clasts (CHRO-1 and CHRO-9) and red colored quartz-rich sandstone clasts (CHRO-2, CHRO-5, CHRO-7, and CHRO-11) with the lowest concentrations were processed. The results of the cosmogenic ^{10}Be and ^{26}Al analyses for the Hasli, Hochwacht, Schartenflue, and Chroobach sites are shown in Table 2. The ^{10}Be/^{9}Be ratios varied from 3.25×10^{-14} to 115.48×10^{-14}. The relative measurement uncertainty of the ^{10}Be/^{9}Be ratios was 1.7–9.7%. The cosmogenic ^{10}Be-concentrations ranged from $(7.92\pm0.81)\times10^{3}$ at./g to $(308.28\pm5.25)\times10^{3}$ at./g. The contribution of the blank correction was 0.2–7.6%. The total Al concentrations varied from 0.32 mg to 9.53 mg, and from 6 to 191 ppm, respectively. The ^{26}Al/^{27}Al ratios ranged from 2.88×10^{-14} to 50.68×10^{-14}. The relative uncertainty of the ^{26}Al/^{27}Al measurements was 1.1–4.5%. The ^{26}Al concentrations ranged from $(41.01\pm1.84)\times10^{3}$ at./g to $(1066.03\pm11.73)\times10^{3}$ at./g. Although samples were processed with total Al concentrations larger than 50 ppm, there was no detectable influence on the final ^{26}Al concentrations, which is due to the new developed MILEA AMS-facility measuring ^{26}Al/^{27}Al and ^{10}Be/^{9}Be ratios with higher efficiency (Maxeiner et al., 2019). The ^{26}Al/^{10}Be ratios ranged from 2.64 ± 0.08 to 7.18 ± 0.52 (Fig. 13; Table 2).

The isochron-burial ages were calculated using the code provided by Erlanger et al., (2012; personal communication with Darryl Granger) using the ratio of 7.6 ± 0.8 (Table 3). For the Schartenflue site, an age of 1.3 ± 0.1 Ma was calculated (Fig. 14a). The Hochwacht site yielded an age of 2.6 ± 0.1 Ma (Fig. 14b). For the Hasli site, an age of 1.3 ± 0.1 Ma was calculated (Fig. 14c). An age of 1.8 ± 0.1 Ma was obtained for the Chroobach site (Fig. 14d). To estimate the contribution of the post-burial production in the measured ^{10}Be and ^{26}Al concentrations, we calculated the isochron-burial ages using the St, Lm, and LSDn, which did not alter the isochron-burial age. In addition, the age calculation with the Code of Bender et al. (2016) yielded the same age as the ones calculated with the code of Erlanger et al., (2012; in personal communication with Darryl Granger). This implies that the post-burial production at our study sites is negligible.

5 Discussion

We first defined the provenance of the Deckenschotter deposits at the study sites, then, established a new chronostratigraphy based on the isochron-burial ages from Chroobach and Irchel. Finally, we combined the provenance, transport mechanism, depositional environment, and the depositional age to reconstruct the landscape evolution and the changes in base level during the early Pleistocene.

5.1 Provenance of the Deckenschotter deposits

As the Deckenschotter deposits are defined as glaciofluvial sediments deposited proximal to the glacier margin, the clast petrology indirectly yielded information about the paleoglacier, which transported fresh gravels from the Alps, as well as reworked material along its flow path. We compared the petrographic results from Irchel with those of Claude et al. (2019) and Graf (1993) (Fig. 8). This comparison enabled us to identify the following compositional classes: (1) Steig Gravel at the Steig and Hasli sites; (2) Irchel Gravel at the Hochwacht, Hütz, Strengebrunnen, Ebni, Grossrüti, and Amslerboden localities; (3) Langacher Gravel at the Schartenflue site; and (4) Forenirchel Gravel at the Schaffhauser Buck, Wilemer Irchel, and Brudergarten sites. All the sample sets analyzed for this study comprise different types of limestone and vein quartz, which are lithologies being abundant across the Alps and therefore do not pinpoint a provenance (Pfiffner, 2010; swisstopo, 2005; Weissert & Stössel, 2010). Instead key lithologies and dolomite,

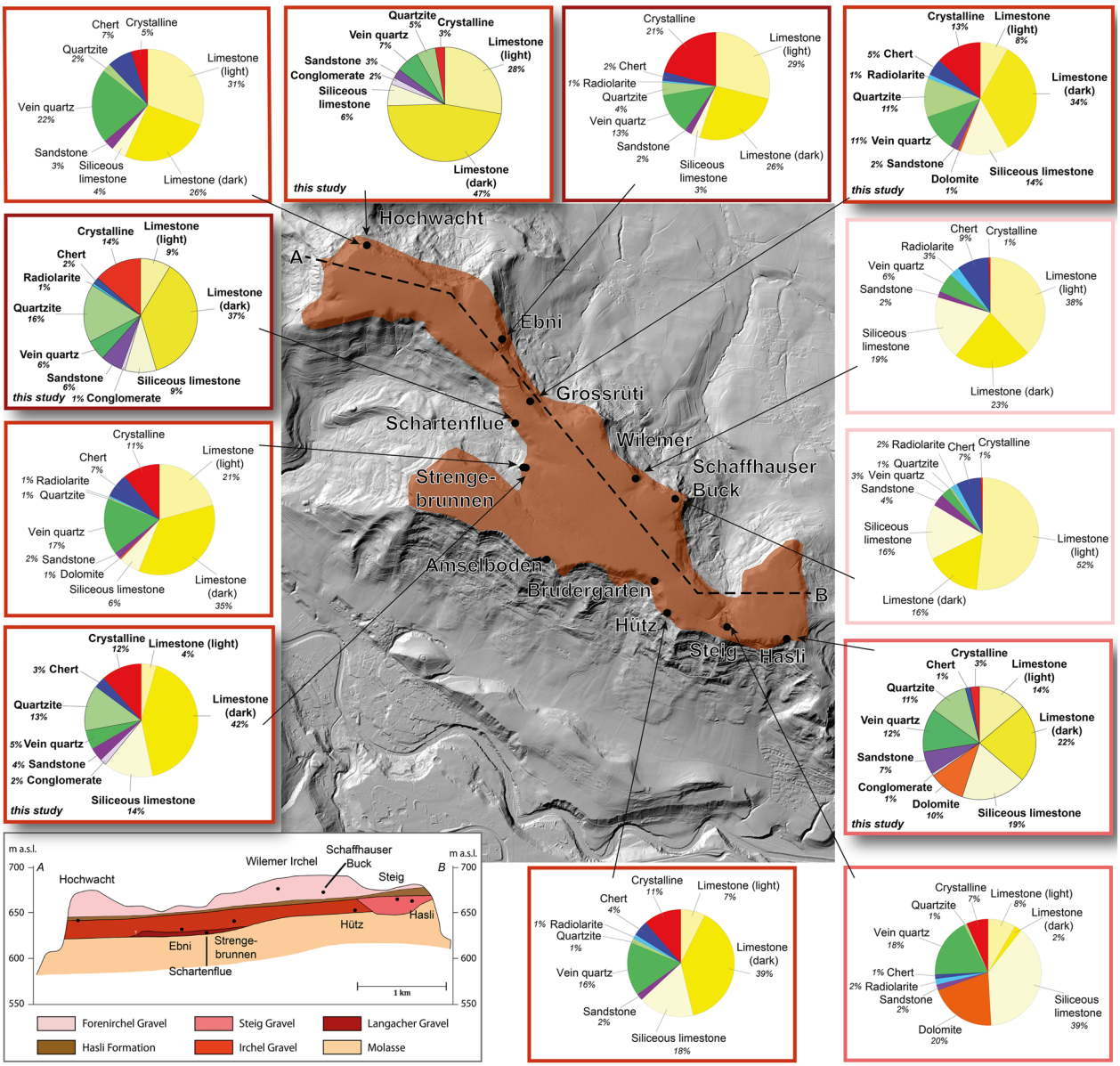

Fig. 8 Clast petrography of the gravels analysed at Irchel and their locations on the map and the cross-section A–B (this study and after Claude et al., 2019). Please note that colour scale on the frames of the pie charts refers to the morphostratigraphy and the formations proposed by Graf (1993)

could suggest an origin of the gravels in the eastern Central to the Eastern Alps transported to the northern Alpine Foreland by the Linth and Rhaetian paleoglaciers, which also reworked parts of the Molasse bedrock. Verrucano, found in all sample sets, currently outcrops in the eastern Central Alps (swisstopo, 2005). In addition, Verrucano is considered a key lithology of the Linth Lobe (Du Pasquier, 1891; Frei, 1912a; Hantke, 1980). Larger volumes of dolomite are exposed in the eastern Central Alps, whereas smaller volumes are found in the Valaisian Alps. Besides the Alps, dolomite can also be reworked from the Molasse, especially from the Hörnli alluvial fan in the Thur Valley (Gasser & Nabholz, 1969; Pavoni, 1957). Quartzite occurs in the Valaisian Alps or in the eastern Central Alps (Sartori et al., 2006). Furthermore, they are also found in the northern Alpine Foreland as a component of the conglomerates in the Molasse (Matter, 1964; Pavoni, 1957). Based on the measured paleoflow directions at the study sites, the geographical location of Chroobach and Irchel, and the absence of key lithologies

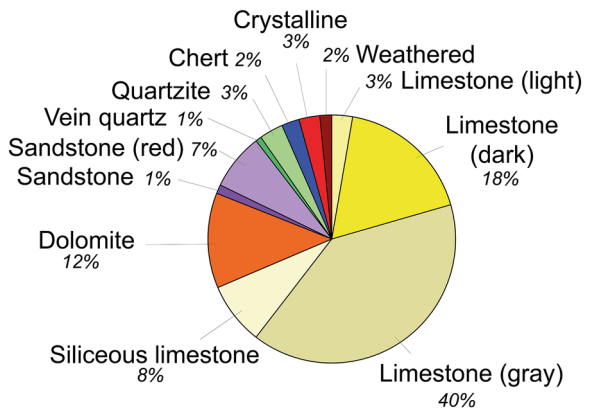

Fig. 9 Clast petrography of the gravels analysed at Chroobach

from the Rhone paleoglacier, the Valaisian Alps as a provenance for these Deckenschotter can be excluded. Furthermore, as there are no key lithologies are present from the Aare and Reuss paleoglaciers, the western Central and the Central Alps could be excluded as origin.

The morphometry of the sediments at the Schartenflue, Hochwacht, Hasli, Strengebrunnen, Grossrüti, and Chroobach sites point towards a glacial to glaciofluvial influence. At all sites, at least about half of the clasts show Z_i values between 150 and 300, which indicates a deposition in the proximity of glaciofluvial environments (Cailleux & Tricart, 1959; Schlüchter, 1976). Around 15–20% of the clasts at the Schartenflue, Chroobach, Grossrüti, and Strengebrunnen sites and around 5% at the Hasli and Hochwacht sites point towards a glacial

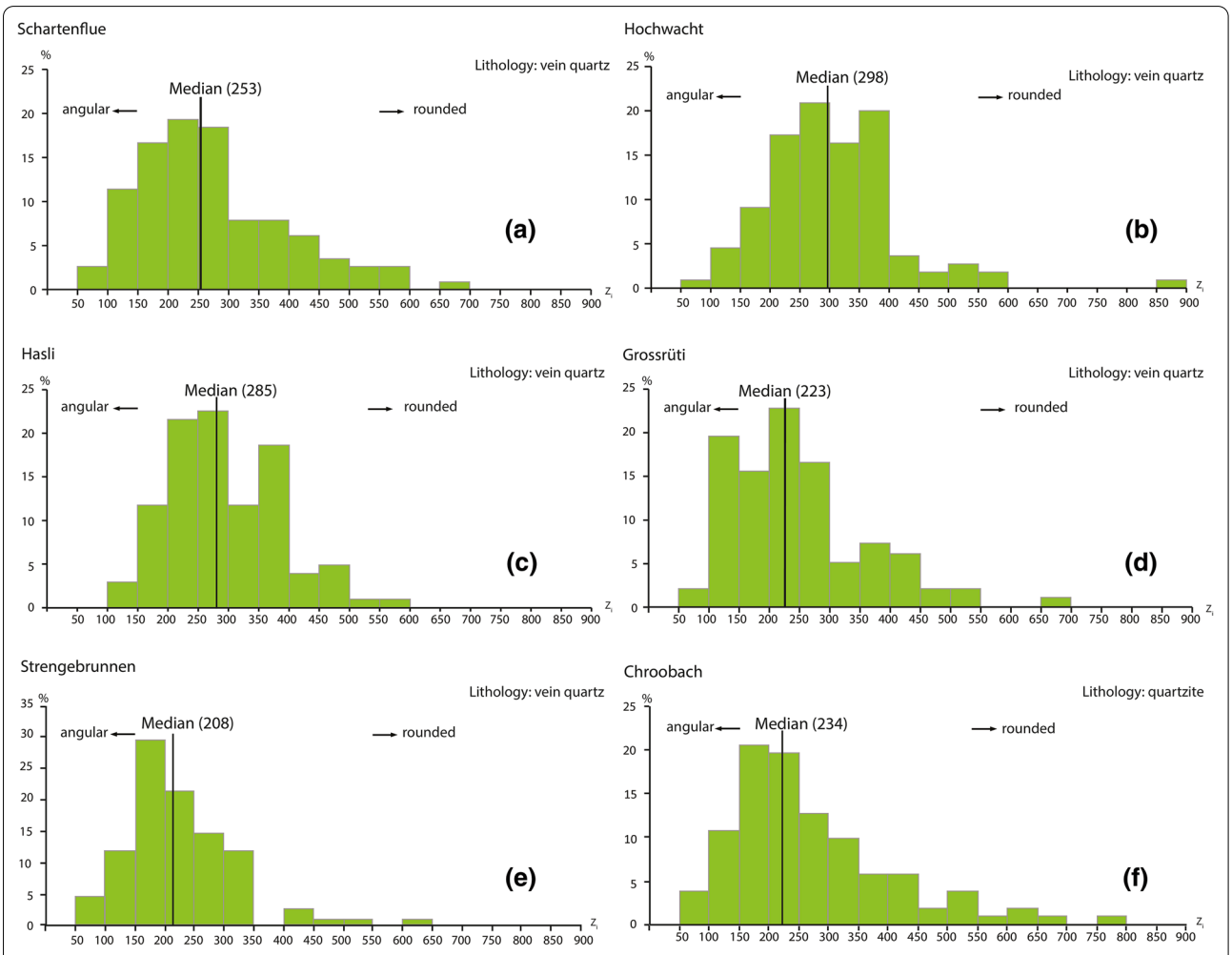

Fig. 10 Roundness index histograms at the study sites: **a** Schartenflue; **b** Hochwacht; **c** Hasli; **d** Grossrüti; **e** Strengebrunnen; and **f** Chroobach

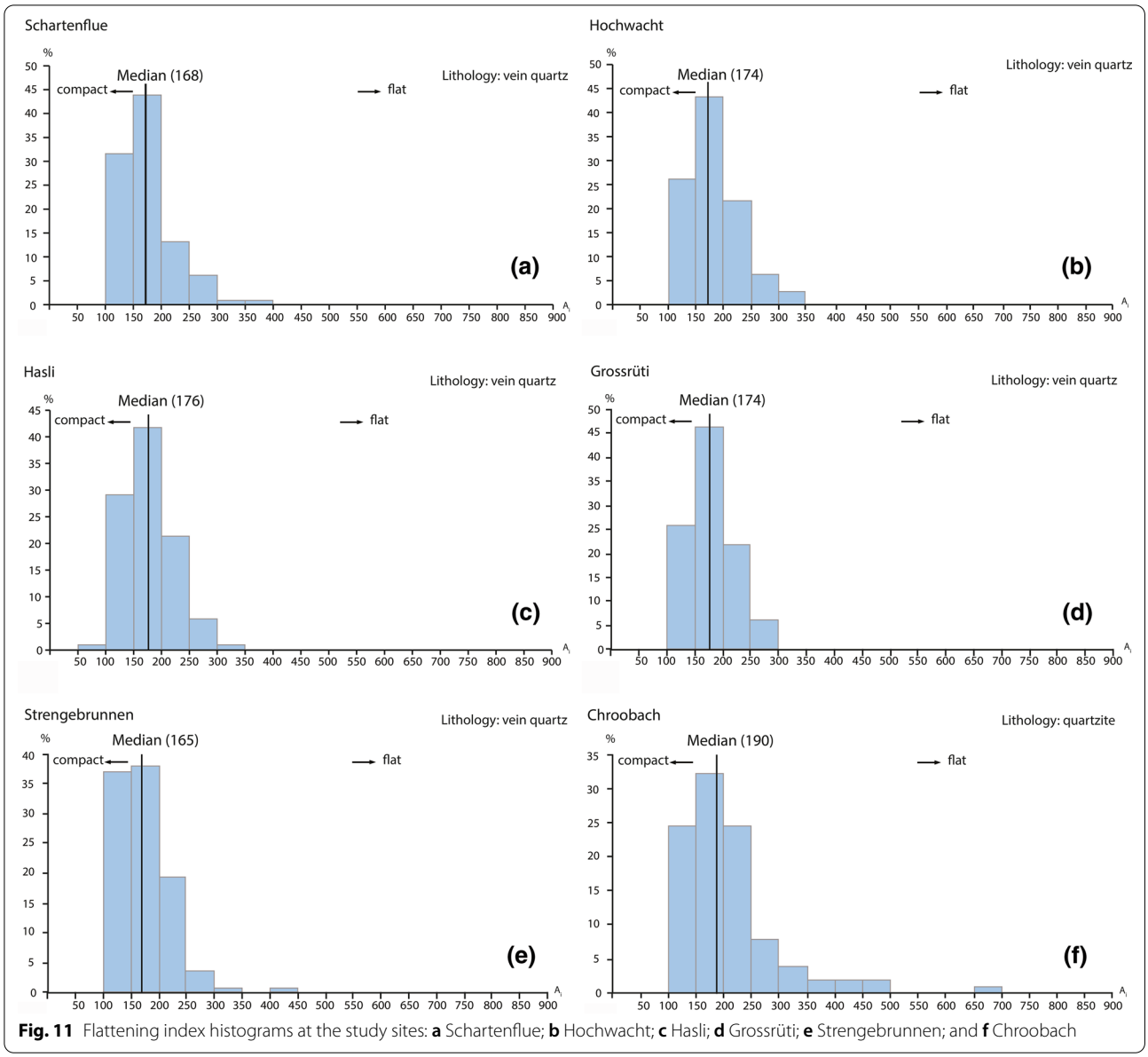

Fig. 11 Flattening index histograms at the study sites: **a** Schartenflue; **b** Hochwacht; **c** Hasli; **d** Grossrüti; **e** Strengebrunnen; and **f** Chroobach

transport, as their Z_i values are between 50 and 150 (Cailleux & Tricart, 1959; Schlüchter, 1976). The values above 300 likely represent better rounded clasts and therefore suggest either reworking or a fluvial transport (Schlüchter, 1976). The values of the flattening index indicate a compact shape of the clasts, which can be interpreted as a glacial to glaciofluvial transport. Based on the results of the sediment analyses, we conclude that the Deckenschotter sediments were transported to the northern Alpine Foreland by glaciers and were then further transported by meltwater.

5.2 Chronostratigraphy of the Deckenschotter

Based on (1) the clast petrographical analyses by Graf (1993), Claude et al., (2019) and this study, and (2) the ages based on the cosmogenic nuclides from the study of Claude et al. (2019) and this study, we propose the following chronostratigraphy (Fig. 15). The Irchel Gravel at the Hochwacht site located on top of the Molasse was dated to 2.6 ± 0.1 Ma (Fig. 15). This age is not in agreement with the Irchel Gravel age at Hütz (0.9 ± 0.2 Ma), which indicates that the lithostratigraphy does not provide any information about their depositional timing although they show the same clast petrographical composition. Based on the isochron-burial age, we assigned the Irchel

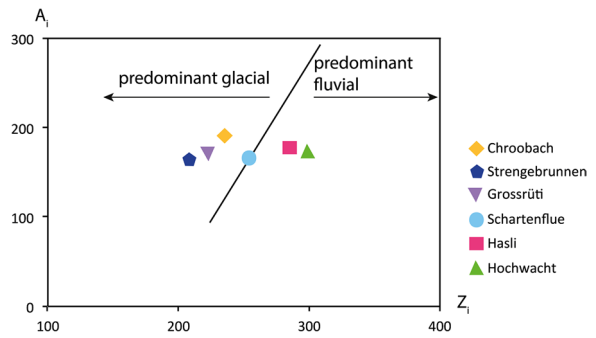

Fig. 12 Median value of the roundness indices Md(Z_i) plotted against median value of the flattening indices Md(A_i). The black line indicates the transition from fluvially dominated to glacially dominated transport (after Schlüchter, 1976)

Gravel at Hütz, Ebni, Grossrüti, and Strengebrunnen to a separate unit called the "Ebni Gravel." The Irchel Gravel represents the oldest deposits and likely covered a large part of the Irchel. At the Amselboden site, the clast petrography was similar to those at Hochwacht, Strengebrunnen, and Hütz. We attribute the Amselboden site to the Irchel gravel due to its topographic location. On top of the Irchel Gravel, the Hasli formation was deposited, consisting of fine-grained sediments. The Hasli formation was biostratigraphically dated to MN17 (2.0–1.8 Ma; Cuenca-Bescos, 2015). The ages of the mammal fossils and the isochron-burial ages are contradictory, as the fossils are older than the dated Steig Gravels underlying the Hasli formation. These few large intact fossils might have been reworked as a result of transport over a short

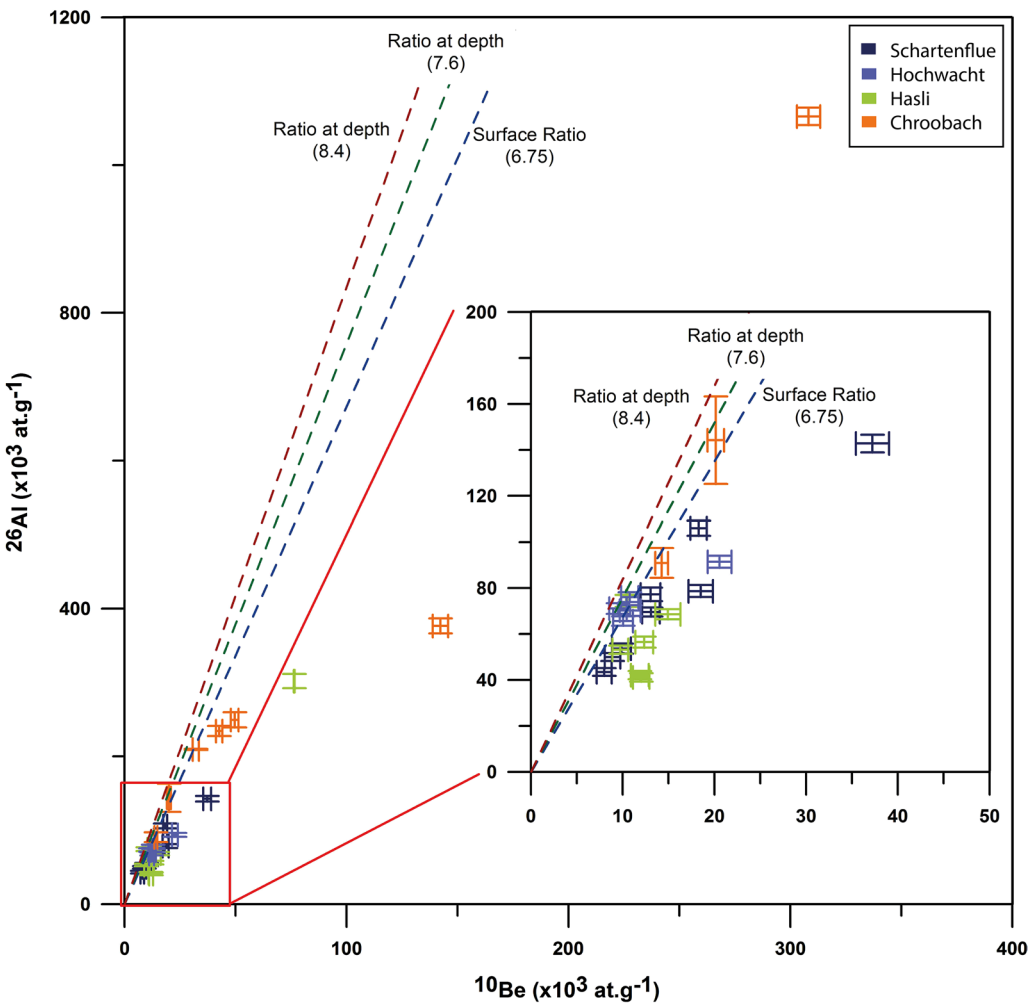

Fig. 13 Measured cosmogenic ^{10}Be concentrations plotted against measured cosmogenic ^{26}Al concentrations. The dashed lines mark the initial ^{26}Al/^{10}Be ratios at the surface (6.75) and at depth (7.6 and 8.4)

Table 3 Calculated isochron-burial ages for the four sites using an initial ratio of 7.6 ± 0.8

Site	Age calculated with the code of Granger (pers. com.) Ratio 7.6 ± 0.8
Irchel Hasli	1.3 ± 0.1 Ma
Irchel Hochwacht	2.6 ± 0.1 Ma
Irchel Schartenflue	1.3 ± 0.1 Ma
Chroobach	1.8 ± 0.1 Ma

distance in a very fine-grained sediment clast. Except for potential reworking, we cannot provide a plausible explanation as to why the mammal fossils are older than the underlying gravels. The Forenirchel Gravel, which was dated to $2.8^{+1.8}_{-1.0}$ Ma (4σ) at the Wilemer Irchel site (Claude et al., 2019), was deposited on top of the Hasli formation (Fig. 15). As the clast petrography from the Wilemer Irchel, Schaffhauser Buck, Brudergarten, and a site located above the Hasli formation at the Hochwacht site all exhibit similar provenances, they were classified into the Forenirchel Gravel.

The 1.3 ± 0.1 Ma Langacher Gravel at the Schartenflue site could have been deposited in the Ebni Channel on top of the Molasse at the end of an incision phase that occurred to create space for deposition. The Langacher Gravel was likely thicker than today. A degradation phase after ca. 1.3 Ma must have eroded the gravel, causing its preservation only as a relict deposit. During this phase, a second channel (Hütz Channel) was also created in the southeastern part of Irchel. At ca. 1 Ma, the Ebni Gravel was deposited in two broad channels: the one indicated by the Strengebrunnen, Grossrüti, and Ebni sites and the other outcropping at Hütz (0.9 ± 0.4 Ma). Later, the Hütz Channel in the southeast was cut by the Steig Channel (cf. Graf, 1993) where the Steig Gravel was deposited at the Hasli (1.3 ± 0.1 Ma) and Steig (0.9 ± 0.2 Ma) sites. In addition, both sites had northward paleoflow directions. These lines of evidence suggest the presence of at least six sub-units at Irchel (Irchel Gravel, Forenirchel Gravel, Langacher Gravel, Ebni Gravel, Steig Gravel, and the Hasli formation), which indicate deposition by cut-and-fill cycles (Fig. 15). This dynamic environment of cut-and-fill sequences at Irchel does not appear to be a local phenomenon, but could also be valid for the other Deckenschotter sites. In addition, these cut-and-fill sequences imply

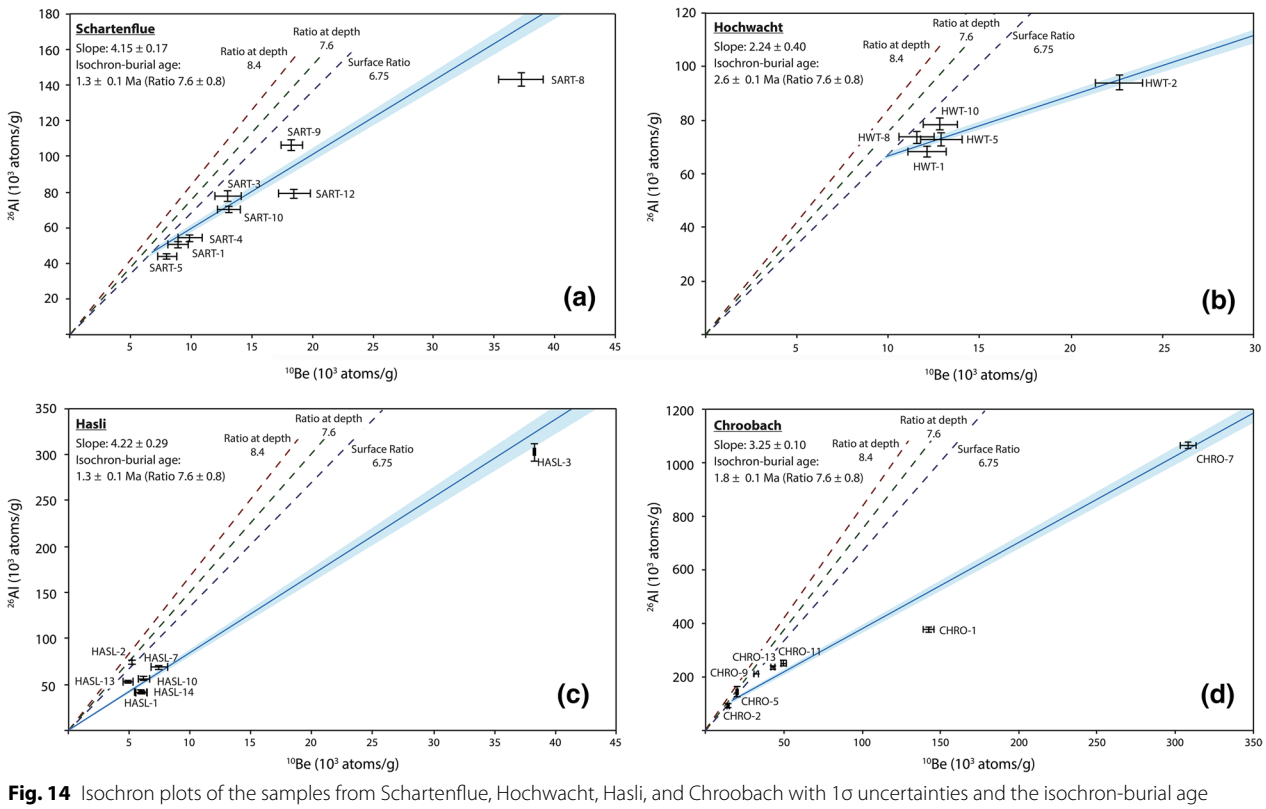

Fig. 14 Isochron plots of the samples from Schartenflue, Hochwacht, Hasli, and Chroobach with 1σ uncertainties and the isochron-burial age calculated with initial ratio of 7.6 ± 0.8. The blue line shows the best-fit isochron line and the light blue envelope the 1σ solution space

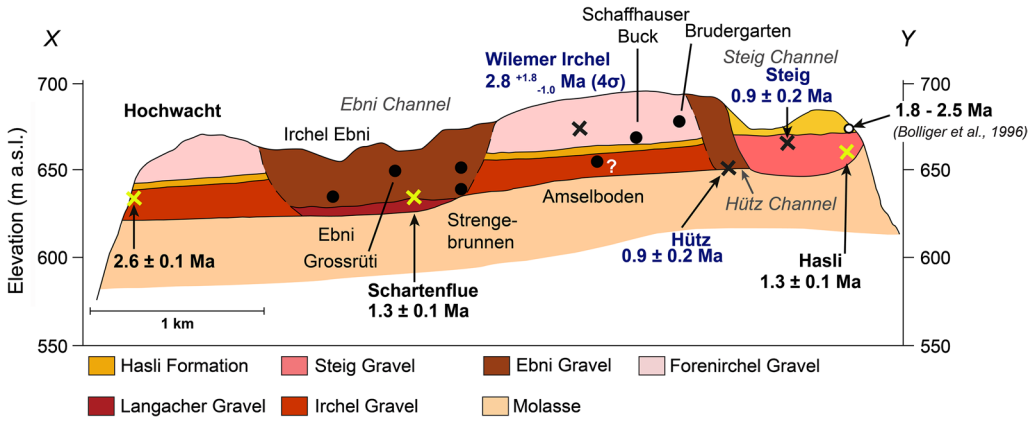

Fig. 15 Cross-section X–Y showing the reconstructed stratigraphy based on the existing and new established cosmogenic nuclide chronology as well as on the clast petrography (modified after Graf, 1993). For the position of the cross-section, please refer to Fig. 2

that sediments of different ages are located at the same topographic elevation. Therefore, using the topographic elevation to constrain the chronostratigraphy can be misleading. Therefore, we prefer to use the term Deckenschotter, as the separation into HDS and TDS based on the morphostratigraphy seems not appropriate to classify and describe these cut-and-fill sequences.

At Irchel, the sub-units exhibited very similar petrographic compositions but had different ages. This can be observed at Hochwacht, where the Irchel Gravel exhibits a very similar clast petrography to that of the Ebni Gravel at Hütz and Strengebrunnen (Fig. 8). Their isochron-burial ages differed, as the Irchel Gravel at Hochwacht was dated to 2.6 ± 0.1 Ma, while the Ebni Gravel at Hütz was dated to 0.9 ± 0.4 Ma (Fig. 15). This result implies that a similar clast petrography does not necessarily indicate similar ages. It also indicates that the catchments were relatively constant at the time of Deckenschotter deposition. This is in agreement with drainage reconstructions that indicated static river catchments (Kuhlemann & Rahn, 2013). The Irchel Gravel, Forenirchel Gravel, Langacher Gravel, and Ebni Gravel span a period of approximately 1.5 Ma and all exhibit imprints from the Linth Lobe. At the Stadlerberg, Feusi, and Siglistorf sites, the situation seems to be similar. At Irchel, with the deposition of the Steig Gravel at ca. 1 Ma, an initial change in the catchment may be inferred, as the relative abundance of dolomite was higher than in the other units.

The detailed analyses of the Deckenschotter deposits at the study sites and the existing Deckenschotter

Table 4 Chronology of the Swiss Deckenschotter sites

Site	Morphostratigraphic unit	Cosmogenic Nuclide	Age (Ma)	Source
Chroobach	HDS	^{10}Be and ^{26}Al	1.8 ± 0.1	This study
Irchel Steig	HDS	^{10}Be and ^{26}Al	0.9 ± 0.1	Claude et al. (2019)
Irchel Hütz	HDS	^{10}Be and ^{26}Al	0.9 ± 0.2	Claude et al. (2019)
Wilemer Irchel	HDS	^{10}Be	$2.8^{+1.8}_{-1.0}$ (4 s)	Claude et al. (2019)
Hasli	HDS	^{10}Be and ^{26}Al	1.3 ± 0.1	This study
Hochwacht	HDS	^{10}Be and ^{26}Al	2.6 ± 0.1	This study
Schartenflue	HDS	^{10}Be and ^{26}Al	1.3 ± 0.1	This study
Stadlerberg	HDS	^{10}Be	$2.4^{+2.3}_{-1.2}$ (3 s)	Claude et al. (2019)
Siglistorf	HDS	^{10}Be and ^{26}Al	1.5 ± 0.1	Akçar et al. (2017)
Feusi	HDS	^{10}Be and ^{26}Al	1.3 ± 0.1	Recalculated from Knudsen et al. (2020)
Tromsberg	HDS	^{10}Be and ^{26}Al	1.5 ± 0.1	Recalculated from Knudsen et al. (2020)
Iberig	TDS	^{10}Be and ^{26}Al	0.9 ± 0.1	Recalculated from Knudsen et al. (2020)

Confidence levels of the modelled depth-profile ages are indicated in parentheses. Reported isochron-burial ages are calculated based on a ^{26}Al/^{10}Be surface ratio of 7.6 ± 0.8 after Akçar et al. (2017) within 1σ uncertainty

HDS upper cover gravels, *TDS* lower cover gravels

chronologies from other sites indicate that these gravel units were deposited during three accumulation phases (Table 4). This finding, combined with the existing sedimentological data and cosmogenic nuclide geochronology, strengthens the interpretation of the Deckenschotter deposits as cut-and-fill sequences (cf. Claude et al., 2019). The first Deckenschotter accumulation phase occurred at ca. 2.5 Ma, the second at ca. 1.5 Ma, and the third at ca. 1 Ma. The Irchel and Forenirchel Gravels at Irchel and gravels at Stadlerberg ($2.4^{+2.3}_{-1.2}$ Ma) were deposited during the first accumulation phase (Fig. 1). During the second phase, Deckenschotter was deposited at Siglistorf (1.5 ± 0.2 Ma), Feusi (1.3 ± 0.1 Ma), Tromsberg (1.5 ± 0.1 Ma), Irchel (1.3 ± 0.1 Ma; Langacher Gravel), and Chroobach (1.8 ± 0.1 Ma). At the Chroobach site in the area around Lake Constance, the Deckenschotter deposits were dated to 1.8 ± 0.1 Ma. According to Frei (1912b), the Deckenschotter deposits at Herrentisch represent gravels transported by the oldest Rhine Lobe. During the third aggradation phase, the deposition of gravels at Iberig (0.9 ± 0.1 Ma) and Irchel (Steig Gravel and Ebni Gravel) occurred at ca. 1 Ma.

5.3 Cut-and-fill build-up of Deckenschotter

Deckenschotter deposits of different ages are all located at similar topographic elevations (Fig. 16). This implies that the local base level was relatively constant from 2.5 Ma to 1 Ma. Although the base level remained relatively constant over time, local aggradation and incisions were observed. At Irchel, ca. 2.6 Ma, ca. 1.5 Ma, and ca.1 Ma Deckenschotter deposited on top of the Molasse are located at similar elevations (Fig. 15). Recent studies indicate that it is challenging to observe cut-and-fill sequences within gravel units and only age constraints could illustrate the presence of a cut-and-fill architecture (e.g., Steffen et al., 2009; Tofelde et al., 2017). At Irchel the different gravel units were distinguished based on their clast petrographical composition and not on the observed lithological contacts in the field (Claude et al., 2019; Graf, 1993; this study). This implies that their cut-and-fill architecture could only be suggested based on the age constraints of the different gravel units at different locations. To create the cut-and-fill sequences, an almost constant base level and changes in sediment supply or water discharge are required. Clast morphometry indicates that the presence of glaciers in the foreland caused these changes. Based on the results from Irchel, at least five glacial advances can be inferred. The first glacial advance reached close to Irchel at ca. 2.6 Ma, transporting sediment toward the northern Alpine Foreland. Gravel aggradation can be linked to the beginning of a deglaciation as a large amount of glacially transported sediment was transported by meltwater; therefore, the sediment supply increased (Benn & Evans, 1998; Savi et al., 2014). During the first deglaciation stage, the Irchel Gravels were deposited on top of the Molasse bedrock. It is likely that the currently preserved gravels are only remnants and that the deposits were thicker at the time of deposition. Deckenschotter are deposited in braided river systems in a glaciofluvial environment (Claude et al., 2017; Graf, 1993). As braided rivers are characterized by lateral movement, this could also explain why

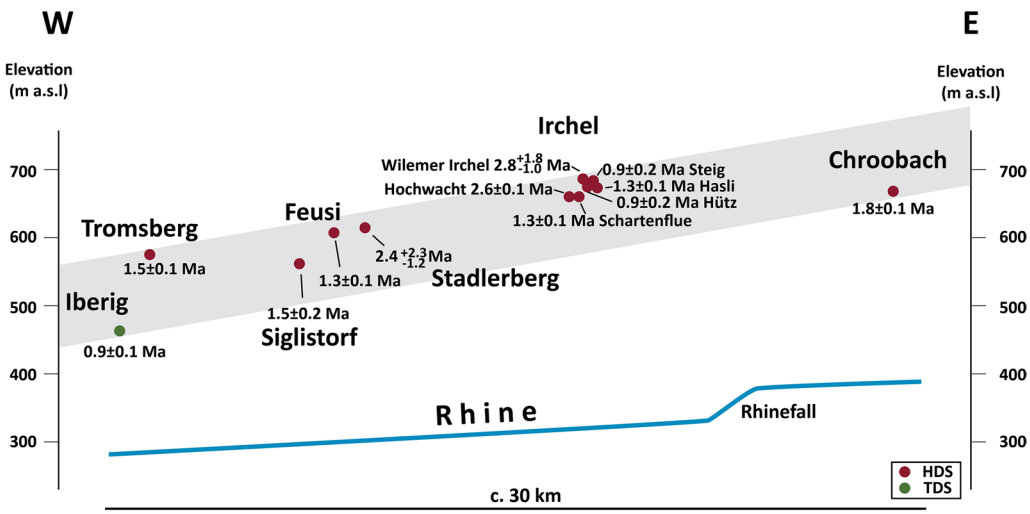

Fig. 16 Elevation vs. distance plot showing positions of the dated Deckenschotter sites (between 2.6 Ma and ca. 1 Ma) and the current base level of the Rhine (modified after Claude et al., 2019). Grey band indicates the base level of the River Rhine during the Deckenschotter times. HDS: Upper Deckenschotter Deposits; TDS: Lower Deckenschotter Deposits

there was negligible or limited incision (Vandenberghe, 2008). In a subsequent phase, glacial retreat and an interglacial period prevailed. Indications for this warm period are the fine-grained sediments in the Hasli formation at Irchel, which overlie the Irchel Gravel and contain mammal fossils, ostracods, or gastropods (Graf, 1993). These fossils indicate that deposition occurred during a warm, more humid period, while some of the fossils point to deposition in a lacustrine environment and not a river (Graf, 1993). Thereafter, glaciers again advanced onto the northern Alpine Foreland, depositing the gravels at Stadlerberg and the Forenirchel Gravel at Irchel. This aggradation phase was then interrupted by a subsequent erosion phase. At Irchel, the Forenirchel Gravel was partially eroded and the incision of the Ebni Channel reached the Molasse. Incision might have been caused by a reduced sediment supply and high meltwater discharge (Ballantyne, 2002; Benn & Evans, 1998). The next glacial advance was observed at Tromsberg, Siglistorf, Feusi, Schartenflue at Irchel, and Chroobach. The Langacher Gravel at Irchel was deposited on top of the Molasse in the Ebni Channel. The third glacial advance was followed by an incision phase that likely partially eroded the Langacher Gravel and formed the Hütz Channel. The fourth glacial advance led to the aggradation of the Ebni Gravel in the Ebni and Hütz channels. Within a short period of time, the next erosion phase occurred, which created space for the Steig Gravel to aggrade as a result of the fifth glacial advance. The five glacial advances and retreats implied by the results of this study must have influenced the bedload and stream power, resulting in three cut-and-fill cycles and the build-up of the Deckenschotter sequence at Irchel.

5.4 Landscape evolution

Prior to the deposition of the first Deckenschotter sediments, the northern Alpine Foreland was characterized by a transient landscape with low relief, wide valleys, and plateau-like hills (Claude et al., 2017, 2019; Gibbard & Lewin, 2009; Kuhlemann & Rahn, 2013; Müller et al., 2002). This topography might have facilitated the advance of glaciers into the northern Alpine Foreland (Müller et al., 2002). According to the sedimentology of the Deckenschotter, it must have been deposited in the proximity of glaciers. This indicates that the glaciers must have reached the northern Alpine Foreland during the periods when the Deckenschotter was deposited. Therefore, we argue that the Deckenschotter gravels at Irchel (Irchel Gravel and Forenirchel Gravel) and Stadlerberg indirectly document the first expansion of glaciers from the central Alps into the Alpine Foreland. Muttoni et al. (2003) and Knudsen et al. (2020) suggested that glaciers reached the southern and northern Alpine Foreland after the Middle Pleistocene Revolution (MPR; ca. 0.9 Ma; Maslin & Ridgwell, 2005). Our results on the contrary indicate an occurrence of foreland glaciations prior to the MPR. The onset of Quaternary glaciation in the northern hemisphere occurred at ca. 2.7 Ma (Gibbard & Lewin, 2009; Maslin & Ridgwell, 2005).

The first Deckenschotter glaciation seems to represent the onset of Quaternary Alpine glaciation to the northern Alpine Foreland, which would correspond to the Marine Isotope Stage (MIS) 100, 102, or 104. The onset of glaciation in the Alpine valleys must have occurred prior to 2.6 ± 0.1 Ma (if glaciers were present) and was then restricted to the Alps. Later glacial advances must have eroded the deposits and features related to the early Alpine glaciation. Drainage reconstructions for the period prior to 2 Ma indicate that the Alpine Rhine was draining eastward into the Danube (e.g., Claude et al., 2019; Liniger, 1966), whereas the base level of the Alpine Rhine was inclined westward (Claude et al., 2019). The rerouting of the Alpine Rhine towards the west is suggested to have occurred at ca. 2.1 Ma (Kuhlemann & Rahn, 2013; Müller et al., 2002).

During the first phase, the Deckenschotter was deposited in a normal stratigraphy without evidence of deep incisions. Phase two was marked by the first cut-and-fill cycle. At the beginning of phase 2, space was created for the subsequent gravel aggradation due to a pulse of erosion. During the second aggradation phase (ca. 1.5 Ma), meltwater from the Rhine and from the Thur, Linth, and Reuss Lobes caused the accumulation of the Deckenschotter at Chroobach, Irchel (Langacher Gravel), Siglistorf, Feusi, and Tromsberg (Graf, 1993, 2009). Based on the presence of an intercalated till layer in the Deckenschotter deposits at Feusi (Graf, 1993), as well as on the clast morphometry indicating a glacial influence on the transportation mechanism (Fig. 12), we suggest that this phase was characterized by glaciers advancing farther onto the northern Alpine Foreland than during the previous phases.

The final phase of Deckenschotter cut-and-fill sequences was marked by a cycle of aggradation and incision at ca. 1 Ma. During this time, meltwater from the Linth and Reuss lobes incised previously deposited Deckenschotter gravels and created accommodation space for the aggradation of fresh material from the eastern Central Alps; for example, the accumulation of gravels at Iberig and in the Steig Channel at Irchel (Graf, 1993; Müller et al., 2002 and references therein). The Deckenschotter deposits were preserved as mesa-type hills. This suggests that the base level dropped and the local relief increased after ca.1 Ma. As a consequence,

enhanced incision prevailed at ca. 1 Ma, which has also been observed at other locations in the Alps. For example, based on dated cave sediments a tenfold increase in erosion after 0.8–1 Ma was observed in the Aare Valley. The delay in the abrupt increase in erosion of around 1 Ma later than the onset of the glaciation in this area might likely be explained by a threshold behavior (Haeuselmann et al., 2007). In addition, the relief of the Rhône Valley increased due to erosion during the past one million years (Valla et al., 2011). This relief increase around 1 Ma was also explained to be induced by the Mid Pleistocene Revolution (MPR) (Claude et al., 2019; Haeuselmann et al., 2007).

6 Conclusions

In this study, we reconstructed the landscape of the Swiss northern Alpine Foreland since the early Pleistocene based on sedimentology and the cosmogenic nuclide chronology of the Deckenschotter. The sedimentology of the Deckenschotter indicates that the deposits originated from the Central and eastern Central Alps, as well as from the Molasse, and that they were deposited in a glaciofluvial environment. The established and existing chronologies suggest that the Deckenschotter deposition occurred in three major accumulation phases at ca. 2.5 Ma, ca. 1.5 Ma, and ca. 1 Ma. During the early Pleistocene, the base level was relatively constant. The cut-and-fill sequences were controlled by changing stream power and bedload due to glacial advances. In addition, the 2.5 Ma glaciofluvial gravels document the first evidence of glaciers in the northern Alpine Foreland. This timing is synchronous with the onset of Quaternary glaciation in the northern hemisphere at ca. 2.7 Ma (Maslin & Ridgwell, 2005).

At Irchel, the results strengthen the evidence for the presence of a more complex cut-and-fill architecture in the Deckenschotter deposits. We suggest that a cut-and-fill structure was present at all of the Deckenschotter deposits, not only at Irchel. Furthermore, subdividing the Deckenschotter deposits that were deposited by cut-and-fill cycles into HDS and TDS based on their morphostratigraphy may not be concurrent with the chronostratigraphy. Thus, deducing a relative chronology based on the morphostratigraphy can be misleading. Therefore, we suggest using Deckenschotter as a collective term instead of HDS and TDS. In addition, we showed in this study that the petrography of the same clasts does not necessarily mean the same age. Using the isochron-burial ages and the petrographic analyses from the Chroobach site, we established an initial chronology of the easternmost Deckenschotter deposited by the Rhaetian paleoglacier in the Swiss northern Alpine Foreland.

Abbreviations

AMS: Accelerator mass spectrometry; HDS: Upper cover gravels; LGM: Last glacial maximum; MN17: Mammal neogene 17; MPR: Mid-Pleistocene revolution; OSM: Miocene Upper Freshwater Molasse; SLHL: Sea level high latitude; TDS: Lower Cover Gravels.

Acknowledgements

We are grateful to Hans Rudolf Graf at Dr. von Moos AG for his support during the preparation of the project and for fruitful discussions. We are thankful to Susan Ivy Ochs at ETH Zurich for her help and support during the sampling campaign. We would like to thank Julia Gaijc at the University of Bern and Serdar Yeşilyurt at the University of Ankara for their assistance and support in the laboratory during sample preparation. We would also like to thank Niklaus Waber, Priska Bähler, and Christopher Pichler at the University of Bern for the ICP measurements. We are also grateful to the Laboratory of Ion Beam Physics accelerator mass spectrometry facility, operated by the Swiss Federal Institute of Technology, Zurich, Switzerland, for the AMS analyses. We acknowledge the constructive comments by the two anonymous reviewers. These contributed to the improvement of the revised manuscript.

Authors' contributions

The research concept was designed by NA and CD. CD and NA conducted field work and collected clast and sediment samples at the four studied Deckenschotter sites. The samples were processed in the laboratory by CD. MC performed the ^{10}Be measurements at the AMS in Zurich. CV and PG performed the ^{26}Al measurements at the AMS in Zurich. CD and NA analyzed and interpreted the data. The manuscript and the figures were drafted by CD with contributions from all authors. All authors read and approved the final manuscript.

Funding

This study was funded by the Swiss Federal Nuclear Safety Inspectorate ENSI (Project No. CTR00314).

Availability of data and materials

All data generated or analysed during this study are included in this published article.

Declarations

Competing interests

The authors declare that they have no competing interests.

Author details

[1]Institute of Geological Sciences, University of Bern, Bern, Switzerland. [2]Laboratory of Ion Beam Physics, ETH Zurich, Zurich, Switzerland.

Received: 20 April 2021 Accepted: 8 February 2022
Published online: 24 March 2022

References

Adelsberger, K. A. (2017). Sedimentology. In A. S. Gilbert (Ed.), *Encyclopedia of Geoarchaeology* (pp. 764–772). Dordrecht, Springer Netherlands. https://doi.org/10.1007/978-1-4020-4409-0_160

Akçar, N., Ivy-Ochs, S., Alfimov, V., Claude, A., Graf, H. R., Dehnert, A., et al. (2014). The first major incision of the Swiss Deckenschotter landscape. *Swiss Journal of Geosciences, 107*(2–3), 337–347. https://doi.org/10.1007/s00015-014-0176-6

Akçar, N., Ivy-Ochs, S., Alfimov, V., Schlunegger, F., Claude, A., Reber, R., et al. (2017). Isochron-burial dating of glaciofluvial deposits: First results from the Swiss Alps. *Earth Surface Processes and Landforms, 42*(14), 2414–2425. https://doi.org/10.1002/esp.4201

Balco, G., & Rovey, C. W. (2008). An isochron method for cosmogenic-nuclide dating of buried soils and sediments. *American Journal of Science, 308*, 1083–1114. https://doi.org/10.2475/10.2008.02

Balco, G., Soreghan, G. S., Sweet, D. E., Marra, K. R., & Bierman, P. R. (2013). Cosmogenic-nuclide burial ages for Pleistocene sedimentary fill in Unaweep Canyon, Colorado, USA. *Quaternary Geochronology, 18*, 149–157. https://doi.org/10.1016/j.quageo.2013.02.002

Ballantyne, C. K. (2002). Paraglacial geomorphology. *Quaternary Science Reviews, 21*, 1935–2017.

Bekaddour, T., Schlunegger, F., Vogel, H., Delunel, R., Norton, K. P., Akçar, N., & Kubik, P. (2014). Paleo erosion rates and climate shifts recorded by Quaternary cut-and-fill sequences in the Pisco valley, central Peru. *Earth and Planetary Science Letters, 390*, 103–115. https://doi.org/10.1016/j.epsl.2013.12.048

Bender, A. M., Amos, C. B., Bierman, P., Rood, D. H., Staisch, L., Kelsey, H., & Sherrod, B. (2016). Differential uplift and incision of the Yakima River terraces, central Washinton State. *Journal of Geophysical Research: Solid Earth*. https://doi.org/10.1002/2015JB012625

Benn, D. I. (2004). Clast Morphology. In D. J. A. Evans & D. I. Benn (Eds.), *A Practical Guide to the Study of Glacial Sediments* (pp. 78–92). Routledge, Taylor & Francis Group.

Benn, D. I., & Ballantyne, C. K. (1994). Reconstructing the transport history of glacigenic sediments: A new approach based on the co-variance of clast form indices. *Sedimentary Geology, 91*, 215–227.

Benn, D. I., & Evans, D. J. A. (1998). *Glaciers and Glaciation* (1st ed.). London: Hodder.

Bini A, Buonchristiani JF, Couterand S, Ellwanger D, Felber M, Florineth D, Graf HR, Keller O, Kelly M, Schlüchter C, Schöneich P. (2009). In *Die Schweiz während des letzteiszeitlichen Maximums (LGM)*, Burkhalter R (Ed). Federal Office of Topography, swisstopo: CH-3084 Wabern, Bern.

Blum, M. D., & Törnqvist, T. E. (2000). Fluvial responses to climate and sea-level change: A review and look forward. *Sedimentology, 47*(Suppl. 1), 2–48. https://doi.org/10.1046/j.1365-3091.2000.00008.x

Boggs, S. (2009). *Petrology of Sedimentary Rocks* (2nd ed.). Cambridge: Cambridge University Press.

Bolliger, T., Fejfar, O., Graf, H., & Kaelin, D. (1996). Vorläufige Mitteilung über Funde von pliozänen Kleinsäugern aus den höheren Deckenschottern des Irchels (Kt. Zürich). *Eclogae Geologicae Helvetiae, 89*(3), 1043–1048.

Borchers, B., Marrero, S., Balco, G., Caffee, M., Goehring, B., Lifton, N., et al. (2016). Geological calibration of spallation production rates in the CRONUS-Earth project. *Quaternary Geochronology, 31*, 188–198. https://doi.org/10.1016/j.quageo.2015.01.009

Boulton, G. S. (1978). Boulder shapes and grain-size distributions of debris as indicators of transport paths through a glacier and till genesis. *Sedimentology, 25*(6), 773–799. https://doi.org/10.1111/j.1365-3091.1978.tb00329.x

Braucher, R., Bourlès, D., Merchel, S., Vidal Romani, J., Fernadez-Mosquera, D., Marti, K., Léanni, L., Chauvet, F., Arnold, M., Aumaître, G., & Keddadouche, K. (2013). Determination of muon attenuation lengths in depth profiles from in situ produced cosmogenic nuclides. *Nuclear Instruments and Methods in Physics Research, Section B: Beam Interactions with Materials and Atoms, 294*, 484–490.

Braucher, R., Merchel, S., Borgomano, J., & Bourlès, D. L. (2011). Production of cosmogenic radionuclides at great depth: A multi element approach. *Earth and Planetary Science Letters, 309*(1–2), 1–9. https://doi.org/10.1016/j.epsl.2011.06.036

Bridgland, D. R. (2000). River terrace systems in north-west Europe: An archive of environmental change, uplift and early human occupation. *Quaternary Science Reviews, 19*(13), 1293–1303. https://doi.org/10.1016/S0277-3791(99)00095-5

Bridgland, D. R., & Westaway, R. (2014). Quaternary fluvial archives and landscape evolution: A global synthesis. *Proceedings of the Geologists' Association, 125*(5–6), 600–629. https://doi.org/10.1016/j.pgeola.2014.10.009

Brook, M. S., & Lukas, S. (2012). A revised approach to discriminating sediment transport histories in glacigenic sediments in a temperate alpine environment: A case study from Fox Glacier, New Zealand. *Earth Surface Processes and Landforms, 37*(8), 895–900. https://doi.org/10.1002/esp.3250

Bull, W. B. (1990). Stream-terrace genesis: Implications for soil development. *Geomorphology, 3*(3–4), 351–367. https://doi.org/10.1016/0169-555X(90)90011-E

Burbank, D. W., & Anderson, R. S. (2011). *Tectonic Geomorphology*. Wiley. https://doi.org/10.1002/9781444345063

Cailleux, A. (1947). L'indice d'émoussé: définition et première application. *Société Géologique de France*, (pp. 250–252)

Cailleux, A., & Tricart, J. (1959). *Initiation à l'étude des sables et galets* (Vol. 3). Centre de Documentation Universitaire Paris

Chandler, D. M., & Hubbard, B. (2008). Quantifying sample bias in clast fabric measurements. *Sedimentology, 55*(4), 925–938. https://doi.org/10.1111/j.1365-3091.2007.00928.x

Chmeleff, J., von Blanckenburg, F., Kossert, K., & Jakob, D. (2010). Determination of the10Be half-life by multicollector ICP-MS and liquid scintillation counting. *Nuclear Instruments and Methods in Physics Research, Section B: Beam Interactions with Materials and Atoms, 268*(2), 192–199. https://doi.org/10.1016/j.nimb.2009.09.012

Christl, M., Vockenhuber, C., Kubik, P. W., Wacker, L., Lachner, J., Alfimov, V., & Synal, H. A. (2013). The ETH Zurich AMS facilities: Performance parameters and reference materials. *Nuclear Instruments and Methods in Physics Research, Section B: Beam Interactions with Materials and Atoms, 294*, 29–38. https://doi.org/10.1016/j.nimb.2012.03.004

Çiner, A., Doğan, U., Yildirim, C., Akçar, N., Ivy-Ochs, S., Alfimov, V., et al. (2015). Quaternary uplift rates of the Central Anatolian Plateau, Turkey: Insights from cosmogenic isochron-burial nuclide dating of the Kizilirmak River terraces. *Quaternary Science Reviews, 107*, 81–97. https://doi.org/10.1016/j.quascirev.2014.10.007

Clark, P., Archer, D., Pollard, D., Blum, J. D., Rial, J. A., Brovkin, V., Mix, A. C., Pisias, N. G., & Roy, M. (2006). The middle Pleistocene transition: Characteristics, mechanisms, and implications for long-term changes in atmospheric pCO_2. *Quaternary Science Reviews, 25*(23–24), 3150–3184.

Claude, A., Akçar, N., Ivy-Ochs, S., Schlunegger, F., Kubik, P. W., Christl, M., et al. (2019). Changes in landscape evolution patterns in the northern Swiss Alpine Foreland during the mid-Pleistocene revolution. *Bulletin of the Geological Society of America, 131*(11–12), 2056–2078. https://doi.org/10.1130/B31880.1

Claude, A., Akçar, N., Ivy-Ochs, S. D., Schlunegger, F., Kubik, P. W., Dehnert, A., et al. (2017). Timing of early Quaternary gravel accumulation in the Swiss Alpine Foreland. *Geomorphology, 276*, 71–85. https://doi.org/10.1016/j.geomorph.2016.10.016

Cuenca-Bescos, G. (2015). The Pleistocene small mammals from Irchel , Switzerland—A taxonomic and biostratigraphic revision. *Expertenbericht im Rahmen der Beurteilung des Vorschlags von mindestens zwei geologischen Stand- ortgebieten pro Lagertyp, Etappe 2, Sachplan geologische Tiefenlager*

Darling, A. L., Karlstrom, K. E., Granger, D. E., Aslan, A., Kirby, E., Ouimet, W. B., et al. (2012). New incision rates along the Colorado River system based on cosmogenic burial dating of terraces: Implications for regional controls on Quaternary incision. *Geosphere, 8*(5), 1020–1041. https://doi.org/10.1130/GES00724.1

Egberts, E., Basell, L. S., Welham, K., Brown, A. G., & Toms, P. S. (2020). Pleistocene landscape evolution in the Avon valley, southern Britain: Optical dating of terrace formation and Palaeolithic archaeology. *Proceedings of the Geologists' Association, 131*(2), 121–137. https://doi.org/10.1016/j.pgeola.2020.02.002

Erlanger, E. D., Granger, D. E., & Gibbon, R. J. (2012). Rock uplift rates in South Africa from isochron burial dating of fluvial and marine terraces. *Geology, 40*(11), 1019–1022. https://doi.org/10.1130/G33172.1

Evans, D. J. A., Shulmeister, J., & Hyatt, O. (2010). Sedimentology of latero-frontal moraines and fans on the west coast of South Island, New Zealand. *Quaternary Science Reviews, 29*(27–28), 3790–3811. https://doi.org/10.1016/j.quascirev.2010.08.019

Foster, G. C., Chiverrell, R. C., Thomas, G. S. P., Marshall, P., & Hamilton, D. (2009). Fluvial development and the sediment regime of the lower Calder, Ribble catchment, northwest England. *CATENA, 77*(2), 81–95. https://doi.org/10.1016/j.catena.2008.09.006

Frei, R. (1912a). Monographie des Schweizerischen Deckenschotters. Beiträge zur Geologischen Karte der Schweiz, N.F. 37

Frei, R. (1912b). Zur Kenntnis des ostschweizerischen Deckenschotters. *Eclogae Geologicae Helvetiae, 11*(6), 814–825. https://doi.org/10.5169/seals-157103

Gasser, U., & Nabholz, W. (1969). Zur Sedimentologie der Sandfraktion im Pleistozän des schweizerischen Mittellandes. *Eclogae Geologicae Helvetiae, 62*(2), 467–516. https://doi.org/10.5169/seals-163708

Gibbard, P. L., & Lewin, J. (2009). River incision and terrace formation in the Late Cenozoic of Europe. *Tectonophysics, 474*(1–2), 41–55. https://doi.org/10.1016/j.tecto.2008.11.017

Graf, H.R. (1993). *Die Deckenschotter der zentralen Nordschweiz*. Ph.D. Thesis. Swiss Federal Institute of Technology Zurich

Graf, H. R. (2009). Stratigraphie und Morphogenese von frühpleistozänen Ablagerungen zwischen Bodensee und Klettgau. *Eiszeitalter Und Gegenwart Quaternary Science Journal, 58*(1), 12–53.

Graf, H. R., & Müller, B. (1999). Das Quartär: Die Epoche der Eiszeiten. In T. Bolliger (Ed.), *Geologie des Kantons Zürich* (pp. 71–95). Ott Verlag.

Granger, D. E., & Muzikar, P. F. (2001). Dating sediment burial with in situ-produced cosmogenic nuclides: Theory, techniques, and limitations. *Earth and Planetary Science Letters, 188*(1–2), 269–281. https://doi.org/10.1016/S0012-821X(01)00309-0

Grotzinger, J., & Jordan, T. (2017). *Allgemeine Geologie*. In Press & Siever (Eds.) (7th Ed.). Springer Spektrum. https://doi.org/10.1007/978-3-662-48342-8

Haeuselmann, P., Granger, D. E., Jeannin, P. Y., & Lauritzen, S. E. (2007). Abrupt glacial valley incision at 0.8 Ma dated from cave deposits in Switzerland. *Geology, 35*(2), 143–146. https://doi.org/10.1130/G23094A

Hantke, R. (1980). *Eiszeitalter. Die jüngste Erdgeschichte der Schweiz und ihrer Nachbargebiete. Band 2, Letzte Warmzeiten, Würm-Eiszeit, Eisabbau und Nacheiszeit der Alpen Nordseite vom Rhein- zum Rhone-System*. Ott Thun

Heuberger, S., Büchi, M., & Naef, H. (2014). NAB 12-20: Drainage system and landscape evolution of northern Switzerland since the Late Miocene. Nagra Arbeitsbericht

Howard, A. D., Fairbridge, R. W., & Quinn, J. H. (1997). Fluvial Terraces—Introduction. In *Geomorphology* (pp. 1117–1124). Berlin, Heidelberg: Springer Berlin Heidelberg. https://doi.org/10.1007/3-540-31060-6_370

Huang, W., Yang, X., Thomson Jobe, J. A., Li, S., Yang, H., & Zhang, L. (2019). Alluvial plains formation in response to 100-ka glacial–interglacial cycles since the Middle Pleistocene in the southern Tian Shan, NW China. *Geomorphology*, *341*, 86–101. https://doi.org/10.1016/j.geomorph.2019.05.013

Knudsen, M. F., Nørgaard, J., Grischott, R., Kober, F., Egholm, D. L., Hansen, T. M., & Jansen, J. D. (2020). New cosmogenic nuclide burial-dating model indicates onset of major glaciations in the Alps during Middle Pleistocene Transition. *Earth and Planetary Science Letters*. https://doi.org/10.1016/j.epsl.2020.116491

Kock, S., Kramers, J. D., Preusser, F., & Wetzel, A. (2009). Dating of Late Pleistocene terrace deposits of the River Rhine using Uranium series and luminescence methods: Potential and limitations. *Quaternary Geochronology, 4*(5), 363–373. https://doi.org/10.1016/j.quageo.2009.04.002

Korschinek, G., Bergmaier, A., Faestermann, T., Gerstmann, U. C., Knie, K., Rugel, G., et al. (2010). A new value for the half-life of 10Be by Heavy-Ion Elastic Recoil Detection and liquid scintillation counting. *Nuclear Instruments and Methods in Physics Research, Section B: Beam Interactions with Materials and Atoms, 268*(2), 187–191. https://doi.org/10.1016/j.nimb.2009.09.020

Kuhlemann, J., & Rahn, M. (2013). Plio-Pleistocene landscape evolution in Northern Switzerland. *Swiss Journal of Geosciences, 106*(3), 451–467. https://doi.org/10.1007/s00015-013-0152-6

Lal, D. (1991). Cosmic ray labeling of erosion surfaces—in situ nuclide production-rates and erosion models. *Earth and Planetary Science Letters, 104*, 424–439.

Lewin, J., & Gibbard, P. L. (2010). Quaternary river terraces in England: Forms, sediments and processes. *Geomorphology, 120*(3–4), 293–311. https://doi.org/10.1016/j.geomorph.2010.04.002

Lewin, J., & Macklin, M. G. (2003). Preservation potential for late quaternary river alluvium. *Journal of Quaternary Science, 18*(2), 107–120. https://doi.org/10.1002/jqs.738

Lindsey, D. A., Langer, W. H., & Van Gosen, B. S. (2007). Using pebble lithology and roundness to interpret gravel provenance in piedmont fluvial systems of the Rocky Mountains, USA. *Sedimentary Geology, 199*(3–4), 223–232. https://doi.org/10.1016/j.sedgeo.2007.02.006

Liniger, H. (1966). Das Plio-Altpleistozäne Flussnetz der Nordschweiz. *Regio Basiliensis, 7*(2), 158–177.

Litty, C., Schlunegger, F., Akçar, N., Lanari, P., Christl, M., & Vockenhuber, C. (2018). Possible climatic controls on the accumulation of Peru's most prominent alluvial fan: The Lima Conglomerate. *Earth Surface Processes and Landforms, 44*(5), 991–1003. https://doi.org/10.1002/esp.4548

Lukas, S., Benn, D. I., Boston, C. M., Brook, M., Coray, S., Evans, D. J. A., et al. (2013). Clast shape analysis and clast transport paths in glacial environments: A critical review of methods and the role of lithology. *Earth-Science Reviews, 121*, 96–116. https://doi.org/10.1016/j.earscirev.2013.02.005

Lukas, S., Graf, A., Coray, S., & Schlüchter, C. (2012). Genesis, stability and preservation potential of large lateral moraines of Alpine valley glaciers—towards a unifying theory based on Findelengletscher, Switzerland. *Quaternary Science Reviews, 38*, 27–48. https://doi.org/10.1016/j.quascirev.2012.01.022

Macklin, M. G., Lewin, J., & Woodward, J. C. (2012). The fluvial record of climate change. *Philosophical Transactions of the Royal Society a: Mathematical, Physical and Engineering Sciences, 370*(1966), 2143–2172. https://doi.org/10.1098/rsta.2011.0608

Margreth, A., Gosse, J. C., & Dyke, A. S. (2016). Quantification of subaerial and episodic subglacial erosion rates on high latitude upland plateaus: Cumberland Peninsula, Baffin Island, Arctic Canada. *Quaternary Science Reviews, 133*, 108–129. https://doi.org/10.1016/j.quascirev.2015.12.017

Maslin, M. A., & Ridgwell, A. J. (2005). Mid-Pleistocene revolution and the 'eccentricity myth.' *Geological Society, London, Special Publications, 247*(1), 19–34. https://doi.org/10.1144/GSL.SP.2005.247.01.02

Matmon, A., Hidy, A. J., Vainer, S., Crouvi, O., Fink, D., Erel, Y., et al. (2015). New chronology for the southern Kalahari Group sediments with implications for sediment-cycle dynamics and early hominin occupation. *Quaternary Research (united States), 84*(1), 118–132. https://doi.org/10.1016/j.yqres.2015.04.009

Matter, A. (1964). Sedimentologische Untersuchungen im östlichen Napfgebiet (Entlebuch—Tal der Grossen Fontanne, Kt. Luzern). *Eclogae Geologicae Helvetiae, 57*(2), 315–428

Maxeiner, S., Synal, H. A., Christl, M., Suter, M., Müller, A., & Vockenhuber, C. (2019). Proof-of-principle of a compact 300 kV multi-isotope AMS facility. *Nuclear Instruments and Methods in Physics Research, Section B: Beam Interactions with Materials and Atoms, 439*(2018), 84–89. https://doi.org/10.1016/j.nimb.2018.11.028

McDougall, I., Brown, F. H., Cerling, T. E., & Hillhouse, J. W. (1992). A reappraisal of the geomagnetic polarity time scale to 4 Ma using data from the Turkana Basin, East Africa. *Geophysical Research Letters, 19*(23), 2349–2352.

Müller, W. H., Naef, H., & Graf, H. R. (2002). *Geologische Entwicklung der Nordschweiz, Neotektonik und Langzeitszenarien Zürcher Weinland*.

Müller, A. M., Christl, M., Lachner, J., Suter, M., & Synal, H. A. (2010). Competitive 10Be measurements below 1 MeV with the upgraded ETH-TANDY AMS facility. *Nuclear Instruments and Methods in Physics Research, Section B: Beam Interactions with Materials and Atoms, 268*(17–18), 2801–2807. https://doi.org/10.1016/j.nimb.2010.05.104

Muttoni, G., Carcano, C., Garzanti, E., Ghielmi, M., Piccin, A., Pini, R., et al. (2003). Onset of major Pleistocene glaciations in the Alps. *Geology, 31*(11), 989–992. https://doi.org/10.1130/G19445.1

Nishiizumi, K. (2004). Preparation of26Al AMS standards. *Nuclear Instruments and Methods in Physics Research, Section B: Beam Interactions with Materials and Atoms, 223–224*(SPEC. ISS.), 388–392. https://doi.org/10.1016/j.nimb.2004.04.075

Nishiizumi, K., Imamura, M., Caffee, M. W., Southon, J. R., Finkel, R. C., & McAninch, J. (2007). Absolute calibration of 10Be AMS standards. *Nuclear Instruments and Methods in Physics Research, Section B: Beam Interactions with Materials and Atoms, 258*(2), 403–413. https://doi.org/10.1016/j.nimb.2007.01.297

Norris, T. L., Gancarz, A. J., Roico, D. J., & Thomas, K. W. (1983). Half-Life of 26Al. *Journal of Geophysical Research, 88*, 331–333.

Du Pasquier, L. (1891). Ueber die Fluvioclacialen Ablagerungen der Nordschweiz. *Beiträge zur Geologischen Karte der Schweiz,* 148

Pavoni, N. (1957). Geologie der Zürcher Molasse zwischen Albiskamm und Pfannenstiel. *Vierteljahresschrift der Naturforschenden Gesellschaft in Zürich,* 102. *Abhandlung, 5*, 117–315.

Penck, A., & Brückner, E. (1909). *Die Alpen im Eiszeitalter*. Leipzig, Germany: H. Tauchnitz

Pfiffner, A. O. (2010). *Geologie der Alpen* (2nd ed.). Haupt Verlag.

Richards, K. (2002). Drainage basin structure, sediment delivery and the response to environmental change. *Geological Society Special Publication, 191*, 149–160. https://doi.org/10.1144/GSL.SP.2002.191.01.10

Sartori, M., Gouffon, Y., & Marthaler, M. (2006). Harmonisation et définition des unités lithostratigraphiques briançonnaises dans les nappes penniques

du Valais. *Eclogae Geologicae Helvetiae, 99*(3), 363–407. https://doi.org/10.1007/s00015-006-1200-2
Savi, S., Norton, K. P., Picotti, V., Akçar, N., Delunel, R., Brardinoni, F., et al. (2014). Quantifying sediment supply at the end of the last glaciation: Dynamic reconstruction of an alpine debris-flow fan. *Bulletin of the Geological Society of America, 126*(5–6), 773–790. https://doi.org/10.1130/B30849.1
Schaller, M., Ehlers, T. A., Stor, T., Torrent, J., Lobato, L., Christl, M., & Vockenhuber, C. (2016). Timing of European fluvial terrace formation and incision rates constrained by cosmogenic nuclide dating. *Earth and Planetary Science Letters, 451*, 221–231. https://doi.org/10.1016/j.epsl.2016.07.022
Schildgen, T., Dethier, D. P., Bierman, P., & Caffee, M. (2002). 26Al and 10Be dating of Late Pleistocene and Holocene fill terraces: A record of fluvial deposition and incision, Colorado Front Range. *Earth Surface Processes and Landforms, 27*(7), 773–787. https://doi.org/10.1002/esp.352
Schlüchter, C. (1976). *Geologische Untersuchungen im Quartär des Aaretals südlich von Bern. Beiträge zur Geologischen Karte der Schweiz N.F. 148*. Wabern, Switzerland: Bundesamt für Landestopographie, swisstopo
Schlüchter, C. (1989). *Eiszeitliche Lockergesteine—Geologie, Genese und Eigenschaften. Ein Beitrag zu den Beziehungen zwischen fundamentaler und angewandter Eiszeitgeologie*. Swiss Federal Institute of Technology Zurich
Sneed, E. D., & Folk, R. L. (1958). Pebbles in the Lower Colorado River, Texas A Study in Particle Morphogenesis. *The Journal of Geology, 66*(2), 114–150.
Spell, T., & McDougall, I. (1992). Revisions to the age of the Brunhes-Matuyama Boundary and the Pleistocene geomagnetic polarity timescale. *Geophysical Research Letters, 19*(12), 1181–1184.
Steffen, D., Schlunegger, R., & Preusser, F. (2009). Drainage basin response to climate change in the Pisco Valley, Peru. *Geology, 37*(6), 491–494.
Stone, J. O. (2000). Air pressure and cosmogenic isotope production. *Journal of Geophysical Research: Solid Earth, 105*, 23753–23759.
swisstopo. (2005). *Tektonische Karte der Schweiz 1:500'000*. Wabern, Switzerland: Federal Office of Topography.
Tofelde, S., Schildgen, T. F., Savi, S., Pingel, H., Wickert, A. D., Bookhagen, B., et al. (2017). 100 kyr fluvial cut-and-fill terrace cycles since the Middle Pleistocene in the southern Central Andes, NW Argentina. *Earth and Planetary Science Letters, 473*, 141–153. https://doi.org/10.1016/j.epsl.2017.06.001
Tu, H., Shen, G., Granger, D., Yang, X., & Lai, Z. (2017). Quaternary Geochronology Isochron $^{26}Al/^{10}Be$ burial dating of the Lantian hominin site at Gongwangling in Northwestern China. *Quaternary Geochronology, 41*, 174–179. https://doi.org/10.1016/j.quageo.2017.04.004
Valla, P. G., Shuster, D. L., & Van Der Beek, P. A. (2011). Significant increase in relief of the European Alps during mid-Pleistocene glaciations. *Nature Geoscience, 4*(10), 688–692. https://doi.org/10.1038/ngeo1242
van Buuren, U., Prins, M. A., Wang, X., Stange, M., Yang, X., & van Balen, R. T. (2020). Fluvial or aeolian? Unravelling the origin of the silty clayey sediment cover of terraces in the Hanzhong Basin (Qinling Mountains, central China). *Geomorphology, 367*, 107294. https://doi.org/10.1016/j.geomorph.2020.107294
Vandenberge, J. (2008). The fluvial cycle at cold-warm transitions in lowland regions: A refinement of theory. *Geomorphology, 98*, 275–284.
Weissert, H., & Stössel, I. (2010). *Der Ozean im Gebirge Eine geologische Zeitreise durch die Schweiz* (2. Auflage.). vdf Hochschulverlag AG an der ETH Zürich
Weltje, G. J., & von Eynatten, H. (2004). Quantitative provenance analysis of sediments: Review and outlook. *Sedimentary Geology, 171*(1–4), 1–11. https://doi.org/10.1016/j.sedgeo.2004.05.007
White, T. S., Bridgland, D. R., Limondin-Lozouet, N., & Schreve, D. C. (2017). Fossils from Quaternary fluvial archives: Sources of biostratigraphical, biogeographical and palaeoclimatic evidence. *Quaternary Science Reviews, 166*, 150–176. https://doi.org/10.1016/j.quascirev.2017.04.016
Whitfield, R. G., Macklin, M. G., Brewer, P. A., Lang, A., Mauz, B., & Whitfield nee Maher, E. (2013). The nature, timing and controls of the Quaternary development of the Rio Bergantes, Ebro basin, northeast Spain. *Geomorphology, 196*, 106–121. https://doi.org/10.1016/j.geomorph.2012.04.014
Zhao, Z., Granger, D., Zhang, M., Kong, X., Yang, S., Chen, Y., & Hu, E. (2016). A test of the isochron burial dating method on fluvial gravels within the Pulu volcanic sequence, West Kunlun Mountains, China. *Quaternary Geochronology, 34*, 75–80. https://doi.org/10.1016/j.quageo.2016.04.003

Publisher's Note